UNIVERSITY OF SOUTHAMPTON

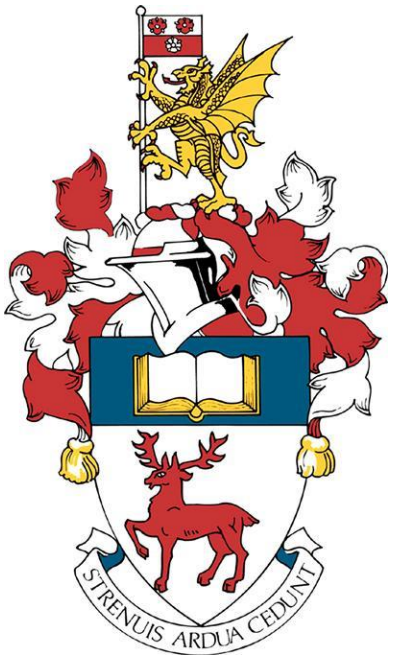

NANOIMPACT TESTING FOR THE SIMULATION OF ENAMEL EROSION CAUSED BY DENTAL AIR ABRASION.

Nixshal Nantakumar

29204488

7 May 2020

Word Count: 10523

Supervisor: Dr Richard Cook

This report is submitted in partial fulfilment of the requirements for the MEng Mechanical Engineering with Biomedical Engineering, Faculty of Engineering and Physical Sciences, University of Southampton.

DECLARATION

I, Nixshal Nantakumar declare that this thesis and the work presented in it are my own and has been generated by me as the result of my own original research.

I confirm that:

1. This work was done wholly or mainly while in candidature for a degree at this University;

2. Where any part of this thesis has previously been submitted for any other qualification at this University or any other institution, this has been clearly stated;

3. Where I have consulted the published work of others, this is always clearly attributed;

4. Where I have quoted from the work of others, the source is always given. With the exception of such quotations, this thesis is entirely my own work;

5. I have acknowledged all main sources of help;

6. Where the thesis is based on work done by myself jointly with others, I have made clear exactly what was done by others and what I have contributed myself;

7. None of this work has been published before submission.

ACKNOWLEDGEMENTS

I would like to thank my supervisor Dr Richard Cook for his guidance, patience and expertise. The countless meetings, discussions and support given by Dr Richard while working on this project was immensely valuable and has given me a new appreciation for experimental research. He is also a massive legend who deserves a pay rise.

Additional thanks to Bethany Harding for her assistance in running experiments, Dr Geoffrey Howell for guidance in the Materials labs and Dr Terry Harvey for guidance in the nCATS facility.

TABLE OF CONTENTS

LIST OF VARIABLES AND ABBREVIATIONS

Symbol	Description
$\dot{\varepsilon}$	Indentation Strain Rate
ANOVA	1 Way Analysis of Variance
CoR	Coefficient of Restitution
D	Contact Footprint Diameter
d	Column Diameter
DEJ	Dentine-Enamel Junction
DH	Dynamic Hardness
E	Elastic Modulus
EB-PVD	Electron Beam Physical Vapour Deposition
E_{impact}	Energy Transfer Per Impact
FOD	Foreign Object Damage
H	Hardness
h	Penetrated Depth
HAP	Hydroxyapatite
h_{max}	Maximum Penetrated Depth
IP	Individual Project
m	Strain Rate Sensitivity Value
SC	Single Crystals
SEM	Scanning Electron Microscope
SRS	Strain Rate Sensitivity
TBC	Thermal Barrier Coating

ABSTRACT

The effect of particle specific variables used in commercial air abrasion systems and their subsequent effect on the erosion behaviour of enamel is not well understood. Nanoindentation methods were used to investigate enamel's mechanical response and erosion behaviour using different particle sizes and flight distances. The erosion behaviours of enamel were linked to strain rate and structural effects such as the keyhole shape of enamel prisms and single-column vs multiple column response. *D/d* ratio, a method to determine erosion mechanisms, was used to compare the behaviour of enamel and columnar thermal barrier coatings. In terms of *D/d* ratio, the erosion mechanisms in enamel were found to be in reverse when compared to thermal barrier coatings.

Chapter 1 INTRODUCTION

Dental caries is a prevalent disease that affects individuals around the world and can reappear throughout the lifetime of a patient [1]. In the United Kingdom, nearly half (49.6%) of the adult population in the United Kingdom has been seen by a National Health Service dentist between 2017 and 2019 [2]. Currently, the high-speed handpiece (dental drill) is the industry standard as a method of removing dental caries. Dentists are fond of the handpiece as it enables them to get a feel for the tissue (healthy enamel or diseased enamel) being drilled. The drawback of this method is that the sound produced leads to a "fear of the drill" and dental anxiety in some patients [3]. Besides the sound, drilling may heat the enamel tissues if they are not cooled properly; this may lead to damage to healthy enamel tissue during an operation.

However, this does not have to be the case as the dental drill isn't the only solution. The removal of stains, caries, and cavities from teeth via air abrasion is becoming increasingly commonplace as modern dental technology is straying away from rotating drills. Air abrasion works by firing an accurate stream of silica or alumina particles at the tooth's surface with sufficient energy to either remove stains from the surface or erode enamel tissue completely. A few advantages of air abrasion include minimal generation of heat, vibration, pressure, reduced need for anaesthesia, reduce risk of fracture, and generally more of the healthy tooth is left behind.

Figure 1: Example of a commercial dental air abrasion unit: AquaCare by Medivance Instruments Ltd., UK. [4]

Air abrasion systems use an air pressure scale to adjust the cutting power without knowledge of the particles' velocity, varying particle size, and different geometries of the particle itself. In practice, dentists relying on the scale to carry out their operations. For example, on a scale of 1-10, 4 is used for removing surface stains and 8 is used to cut into enamel tissue. The particle specific variables that play a role in removing tissue as well as the erosion behaviour of enamel as a result of being hit by these particles are poorly understood. By increasing the level of knowledge on the roles of these variables and their interactions with the tissue, it would augment the control of the air abrasion system.

Enamel tissue is comprised of a columnar microstructure which adds a layer of complexity in understanding its erosion mechanisms, especially regarding the particle sizes and column sizes. However, there have been studies carried out on the erosion mechanisms for other columnar structures, specifically thermal barrier coatings (TBC).

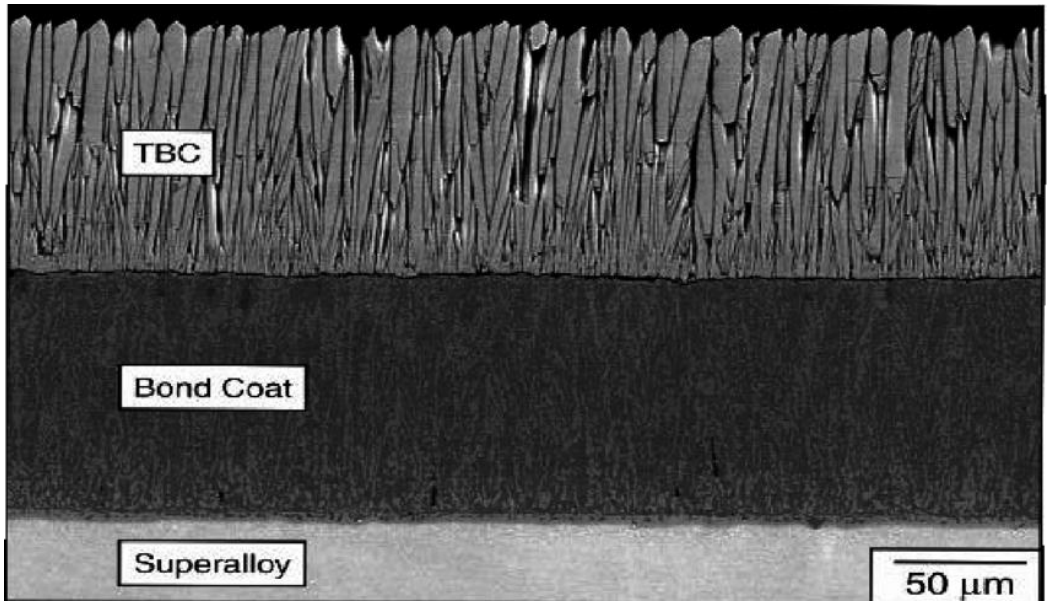

Figure 2: Columnar structure of a thermal barrier coating produced by EB-PVD [5]

The use of TBC systems is steadily increasing in components of the gas turbine engine such as blades, combustors, and nozzles for both military and commercial applications [6]. Some TBC's such as those produced by electron beam physical vapour deposition (EB-PVD) contain a columnar microstructure in their topcoat similar to the columnar structure of enamel.

Owing to this similarity in structure, the erosion behaviours of enamel and their relationship with the erosion behaviours of TBC's are highly interesting and there is a potential of structure-specific effects that overlap between the two distinct materials.

Chapter 2 AIMS AND OBJECTIVES

AIMS

- To investigate the effect of particle geometry and impact energy on the erosion of enamel tissue.
- Investigate the relationship between the erosion behaviour of enamel and columnar thermal barrier coatings.

OBJECTIVES

- Simulate single particle impacts onto enamel using the NanoTest® Vantage (MicroMaterials Ltd., Wrexham, UK) nanoindentation system, using a range of tip (particle) sizes and particle flight distances.
- To study the impact response of enamel to determine the influence of the strain rate and the particle geometry versus the column size on the enamel tissue response.
- To nanoindent and nanoimpact the enamel to compare the hardness response of the enamel under dynamic and quasi-static loading.
- To study the sub-surface damage generated in enamel by particles of different sizes and different impact energies.
- To compare the erosion behaviour of enamel to columnar TBCs and identify any trends between them.

Chapter 3 LITERATURE REVIEW

3.1 ENAMEL AND ITS MICROSTRUCTURE

The human tooth is comprised of 3 distinct regions: enamel, dentine, and pulp within [7, 8]. Enamel is a highly calcified biocomposite [9] material and also the hardest in the human body [10, 11]. By weight, its composition is 92-96% inorganic material, 1-2% organic material, and 3-4% water [12].

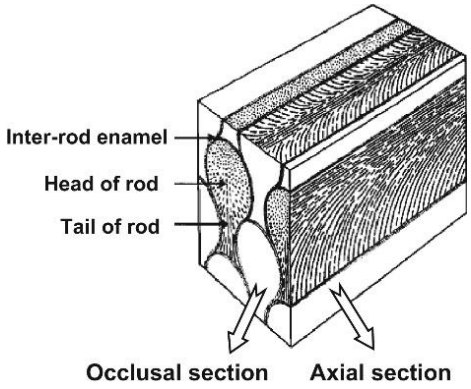

Figure 3: Schematic diagram of enamel microstructure [13].

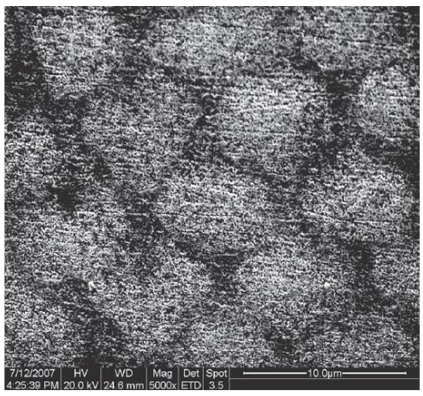

Figure 4: Scanning electron microscope (SEM) image of the surface of the occlusal surface [13].

As shown in Figure 3, enamel consists of aligned, 'keyhole-shape' (shown in Figure 4) enamel prisms/rods, 4-8 μm in diameter, that are perpendicular from the dentine-enamel junction (DEJ) to the tooth surface [14]. Enamel prisms are the basic structural units that form enamel [10]. Each enamel prism contains tightly packed, fibril-like hydroxyapatite (HAP) crystals [14] with a width of 68.3nm and a thickness of 26.3nm [12]. The HAP crystals are separated by a thin layer of enamelin (a protein) which 'glues' and organizes particles into crystals [12]. The protein-rich [12, 14] interface between prisms is called interrod enamel and is mainly a result of the incoherence of combining crystals of different orientations [15].

Bovine enamel was chosen as it emulates the composition and structure of human enamel. The structure does vary between species but enamel always comprises of three hierarchical levels [16] which are:

- Level 1 – HAP particles glued together by enamelin
- Level 2 – Enamel prisms made of aligned HAP crystals (made of HAP particles)
- Level 3 – Enamel prisms with similar orientation form Hunter-Schreger bands [17]

The hierarchical structure of bovine enamel with Hunter-Schreger bands are shown in Figure 5 below. Between Level 1 and Level 2, the HAP particles bonded together by enamelin will self-assemble into nano-fibrils [13] as shown in Figure 5(a). For the reader's clarity: the hierarchy sequence in enamel is HAP particles > nanofibrils > HAP crystals> enamel rods.

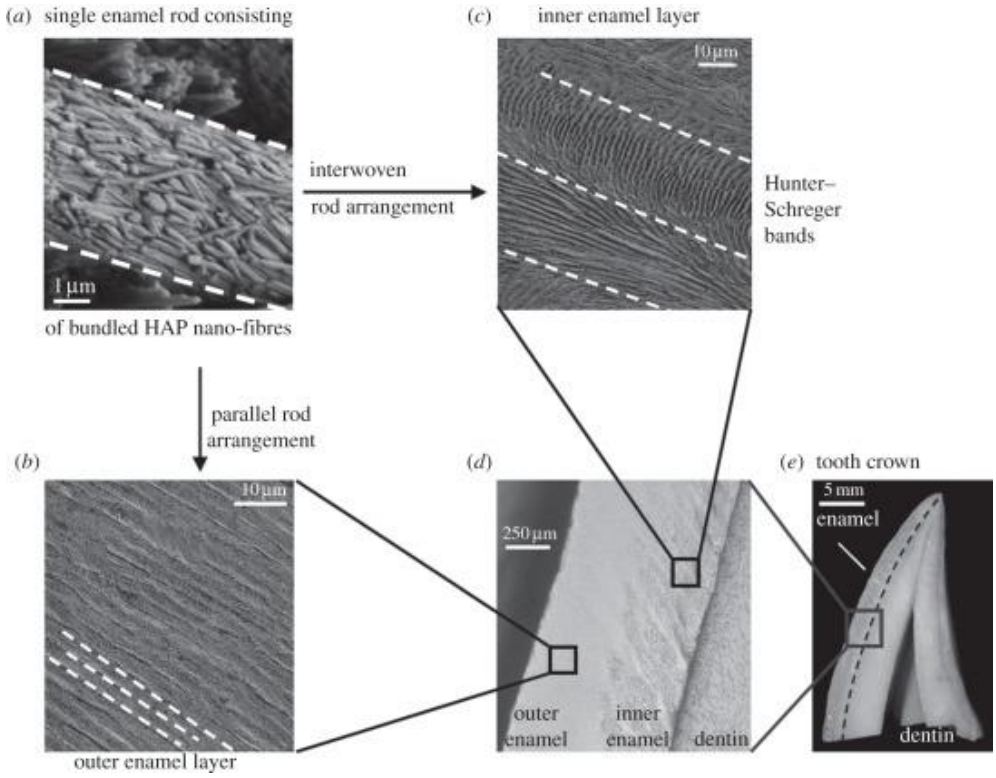

Figure 5: The hierarchical structure of bovine enamel [17].

3.2 EFFECT OF CONTACT ON ENAMEL

Nanoindenters are used to simulate the impact of alumina particles from the air abrasion system on the enamel surface. Therefore it is important to understand how the enamel's structure reacts to contact, via nanoimpacts or nanoindentation.

Zhou and Hsiung [18] carried out a study where the tip radius was set to 50nm, to match the diameter of a single HAP crystal. Since the tip radius and diameter equal, dislocations in 1 enamel prism cannot accommodate deformation. However, deformation of the enamel surface may occur when the HAP crystals move and rotate as shown in Figure 6.

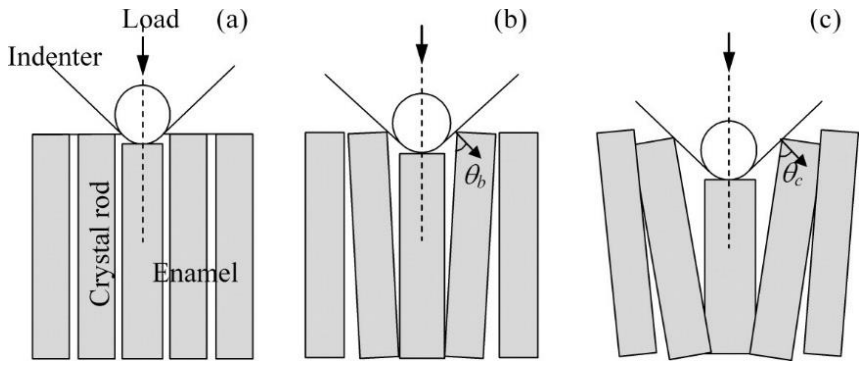

Figure 6: Schematic illustration of the tip-induced realignment of HAP single crystals [18].

Nanoscratch tests carried out by Zheng et al [13] showed that the behaviour of enamel differed to that of artificial hydroxyapatite, even though enamel consists of >92% hydroxyapatite [12]. The nanoscratch tests provided an interesting insight into how material is removed from the enamel surface, with HAP particles being detached from the rods.

Zheng et al observed that at low loads (~5mN), enamel's wear process was mainly down to the collapse of the nano-fibres followed by plastic deformation. HAP particles glued together by enamelin were separated by the action of the normal load of the indenter as shown in Figure E (a). This also caused the size of the HAP particles to decrease.

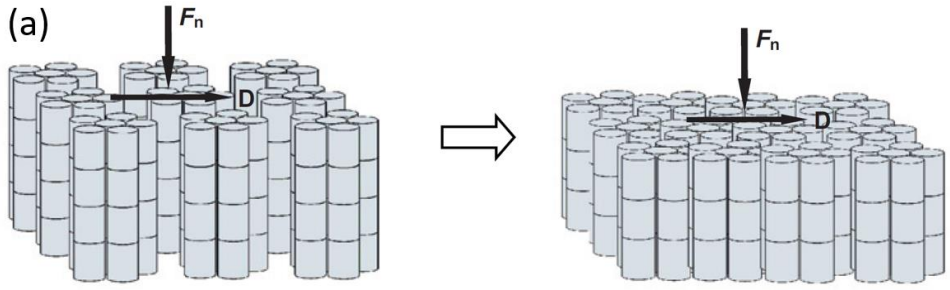

Figure 7: Wear process for enamel at nanofibril level for low loads shows a decrease in size of HAP particles after a normal load is applied [13].

This experiment aims to study the damage generated in enamel by the impacting particles. Nanoindentation testing is suitable as it can measure the properties of the sub micrometre volumes with high accuracy [19].

There are limited studies into the energy dissipation characteristics of enamel. He and Swain have used energy methods to determine if cracking (material loss) occurred based on load-displacement curves [20]. Between spherical and Berkovich indenters, this study noted that a smaller indenter radius produces a higher energy loss at the same contact depth. Energy loss for spherical indenters is a function of the contact strain. At equal contact strains, the spherical indenters have lower energy losses than Berkovich indenters as the latter has a sharper tip and higher associate stresses.

3.3 ROLE OF ORGANIC MATTER WITHIN ENAMEL MICROSTRUCTURE

It is a common theme among all the literature in this review that the microstructure of enamel is a major contributor to its impressive mechanical properties [17-23].

The energy-absorbing capability of enamel is attributed to organic matter present in the enamel structure: the protein-rich region between enamel rods and the enamelin between the HAP particles. He and Swain mention that the protein presence alters the overall properties considerably by providing a softening effect, deflecting cracks, and imparting the enamel with inelastic properties [20]. He and Swain's findings that the protein presence increases enamel's toughness agree with Zheng et al [13]. Deproteinized enamel tissue resulted in the fracture toughness being reduced by up to 40% [24].

3 mechanisms energy loss are proposed. Firstly, fluid flow occurring in the enamelin sheaths allows enamel to act like a "stiff sponge" as described by Fox [25]. Moreno and Zahradnik support this, showing that energy may be dissipated during indentation by forcing the liquid through the interprismatic channels [26], followed by He and Swain who theorize free water located within the protein matrix influences the enamel's compressibility, permeability and ionic conductivity [27]. Secondly, the energy loss can be attributed to sacrificial bonds of the proteins within enamel [28]; this mechanism requires a large amount of energy to break up the peptide bonds found in these proteins [29]. This is supported by research of bone behaviour where energy dissipation during a bone fracture is partially (in bone, micro-cracking is more commonly observed) absorbed by sacrificial bonds [29, 30]. Lastly, an imperfect arrangement of HAP crystals leads to a degustation, where the enamel rods get twisted together and contribute to nanoscale friction which inhibits the recovery of the enamel after unloading, resulting in deformation [31].

3.4 EFFECT ON MECHANICAL PROPERTIES

Bechtle found that mechanical properties decrease by a factor of 2 at each hierarchical level [16], due to the increase in protein content at each level [17]. Depth-dependent mechanical properties of enamel investigated by Zhou shows hardness and elastic modulus incessantly decrease with increasing penetration depth [18]. This concurs with Bechtle's results as the decreasing values are speculated to be linked with the evolution of the microstructure that is caused by the nanoindenter tip. Other properties such as fracture stress (MPa) and fracture strain (%) also seem to decrease with increasing levels of hierarchy [17].

According to Katz [32] and Spears [33], for indentations made parallel to the enamel prisms, the stresses are borne by the stiff HAP crystals where higher hardness and elastic modulus can be

observed. As for indentations made perpendicular to the prisms, the stresses are borne by the low stiffness organic matrix that surrounds the rods. This results in lower hardness and elastic modulus in this direction, indicating anisotropic properties of enamel possibly due to their composite nature.

Enamel also shows viscoplastic and viscoelastic behaviour [21]. Treating the protein and water within enamel as biopolymers, Gao suggested that these viscoelastic and viscoplastic properties stem from the biopolymers' configuration and interactions among the macromolecules [34]. The viscoelastic property of enamel distributes the localized high impact stresses [21]. Staines also reported viscous damping [35] in enamel, possibly due to the pumping of fluids within the narrow channels in the microstructure [26].

Table 1 shown below is a summary of values for elastic modulus and hardness obtained from literature, to visualize comparisons between different studies.

Table 1: Data from literature for elastic modulus and hardness of human enamel from nanoindentation methods.

Author	Maximum depth/load used	Elastic modulus, E (GPa)		Hardness, H (GPa)	
		Occlusal area	Axial area	Occlusal area	Axial area
Habelitz [12]	1500 μN; 300nm	87.5 ± 2.1	72.7 ± 4.4	3.8 ± 0.3	3.3 ± 0.4
Jiang [36]	1600 μN; 300nm	-	10 < E < 80	-	0.5 < H < 5.0
Fong [37]	100 nm	98.3 ± 5.9	95.6 ± 4.9	4.78 ± 0.36	4.53 ± 0.26
Ge [14]	1000μN (prism) 300μN (sheath)	83.4 ± 7.1 (prism) 39.5 ± 4. (sheath)	-	4.3 ± 0.8 (prism) 1.1 ± 0.3 (sheath)	-
Xu [38]	1.9N	98 ± 4	86 ± 3	3.79 ± 0.18	3.50 ± 0.12
Park [39]	5mN, 190nm	84.4 ± 4.4		4.0 ± 0.3	
Elfallah [40]	10mN, 300nm	108 ± 3	-	5.8 ± 0.3	-
Cuy [19]	400nm; 800nm	-	>115 (near surface) <70 (near DEJ)	-	>6 (near surface) <3 (near DEJ)
Willems [41]	-	90.59 ± 16.13		-	
Mahoney [42]	-	-		4.88 ± 0.35	

E and H values reported by Elfallah are highest, but samples used in the study were covered in nail polish [40]. The data for E by Xu and Fong are ~98 GPa while Habelitz and Ge reported ~85 GPa on average. This 12% difference is small and is probably due to different orientations of the sample

leading to a difference in the angle when nanoindentation took place and different depths from the surface.

Ge's results show that the enamel prisms are 2-3 times harder than the organic sheath between prisms. Differences in E and H values between the literature also depend on the hydration of enamel [35]. Cuy also explained variations in values can be attributed to different locations [19] of indentation, whether the indenter hits the prism or interfacial area along with the alignment of the enamel rods itself [36]. Enamel is a biological sample, such differences in measured values are to be expected. From Table 1 the measured values are increasing further away from the DEJ. Zhou reported E and H values decrease by about ~30% as the penetration depth of indenter increases [18]. Shellis and Dibdin suggested that the less-mineralized surface above the DEJ is linked to increased porosity and water that could result in lower E and H [43].

3.5 HYDRATED VERSUS DEHYDRATED ENAMEL TISSUE

Bonte suggests that water exists in enamel in two separate states: free water and strongly bound water [44]. There is a significant change in enamel's properties dehydrated. Local overheating can result in dehydration and changes in the microstructure and chemistry of human teeth [13]. Dehydration of enamel can influence the function of the proteins [21], and as described in Chapter 3.3, proteins and organic matter contribute heavily to the properties of the enamel. Figure 8 shows dehydrated enamel and its susceptibility to microcracking. Dehydrating is avoided by water cooling when grinding/polishing and storing in distilled water when not in use [13, 22, 23, 35, 45, 46].

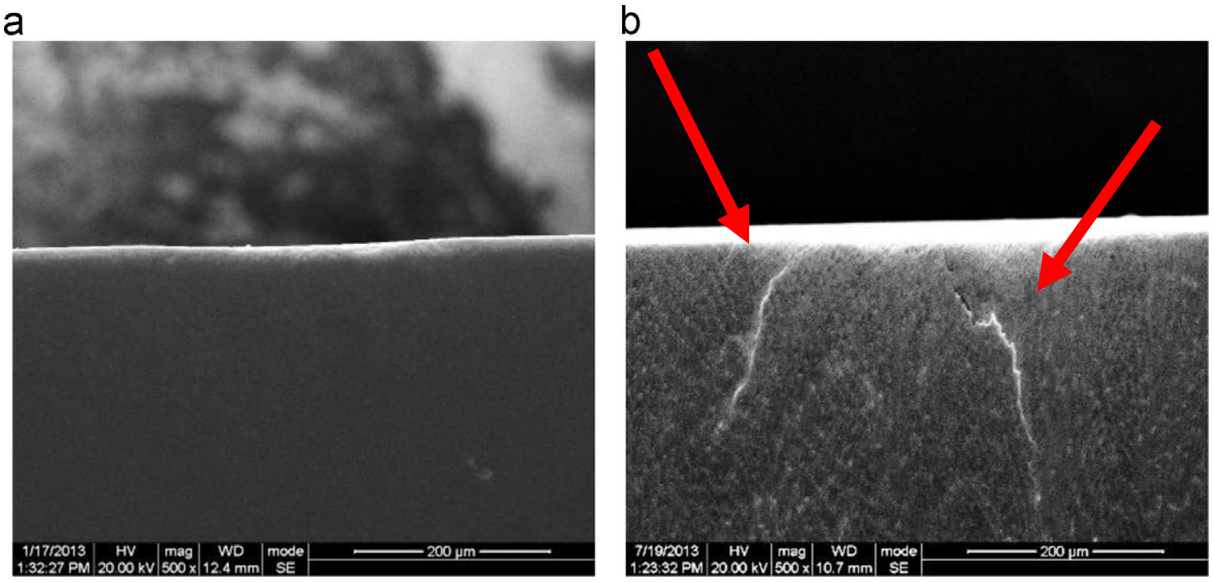

Figure 8: Cross-section of wear scar observed under SEM after 106 cycles;
(a) Wet enamel (b) Dry enamel. Note the obvious microcracks in dry enamel [22].

Table 2 compare several mechanical properties of enamel between a wet state and dry state. Possible explanations from the literature are also included.

Table 2: Data from literature comparing tests between wet and dry enamel samples.

Author	Variable tested	Quantitative result		Reasoning
		Wet	Dry	
Zheng [22]	Wear rate, (cycles)	Decreased after 8.5E5 cycles	Decreased after 5.5E5 cycles	Possible that water content inside enamel prevents impact wear on surface.
Staines [35]	Change in E (10^{10} Pa) with moisture content	6.9	7.8 (18hr) 8.0 (72hr)	Increase in elastic modulus due to loss of water from voids between HAP nanofibers.
Baldassarri [47]	Fracture toughness bb(MPa*$m^{0.5}$) (mid-sagittal plane, transverse plane)	1.57 ± 0.1, 0.57 ± 0.1	1.22 ± 0.1, 0.52 ± 0.1	Assumes that lack of water affects enamel proteins ability to absorb and dissipate impact energy.

Zheng proved a linear relationship between the reduction of fracture toughness and decrease of water content within enamel [22], in agreement with the findings from Yahyazadehfar [24]. Literature that compares the mechanical properties of hydrated/dehydrated enamel and the relationship between the two states is limited.

3.6 STRAIN RATE SENSITIVITY

Spherical indenters allow for different strain rates and quantify parameters such as energy absorption [46]. He and Swain indicate that spherical indentation results in similar indentation strain with Berkovich indentation [46]. Strain rate sensitivity, SRS, is a measure of a parameter/materials strain rate dependence. SRS, quantified as *m*, is explained by Maier-Kiener and Durst as a power-law relationship [48] between the plastic stress (hardness, H is used as indentation stress is directly proportional to the hardness [49]) and applied strain rate shown in Equation 1 below.

$$m = \frac{\partial \ln \sigma}{\partial \ln \dot{\varepsilon}} \sim \frac{\partial \ln H}{\partial \ln \dot{\varepsilon}} = \frac{\partial \ln H_2 - \partial \ln H_1}{\partial \ln \dot{\varepsilon}_2 - \partial \ln \dot{\varepsilon}_1} \qquad \text{Eq. (1)}$$

Zhang showed the hardness of enamel at various strain rates is linked to the creep behaviour of the organic matrix [50]. This is in agreement with He and Swain who place the protein components as the dominant factor in creep behaviour [21]. Ethanol dehydration which impairs protein functionality carried out in a separate experiment by He and Swain further reinforces the previous findings as the creep ability of the sample was significantly limited [27]. SRS of the elastic modulus of enamel would indicate that the protein matrix is influenced by SRS as well.

3.7 COMPARISON BETWEEN ENAMEL AND THERMAL BARRIER COATINGS

The use of thermal barrier coating (TBC) systems is steadily increasing on turbine engine components such as blades and combustors [6]. Some TBC's such as those produced by electron beam physical vapour deposition (EB-PVD) has a columnar microstructure [51] similar to enamel.

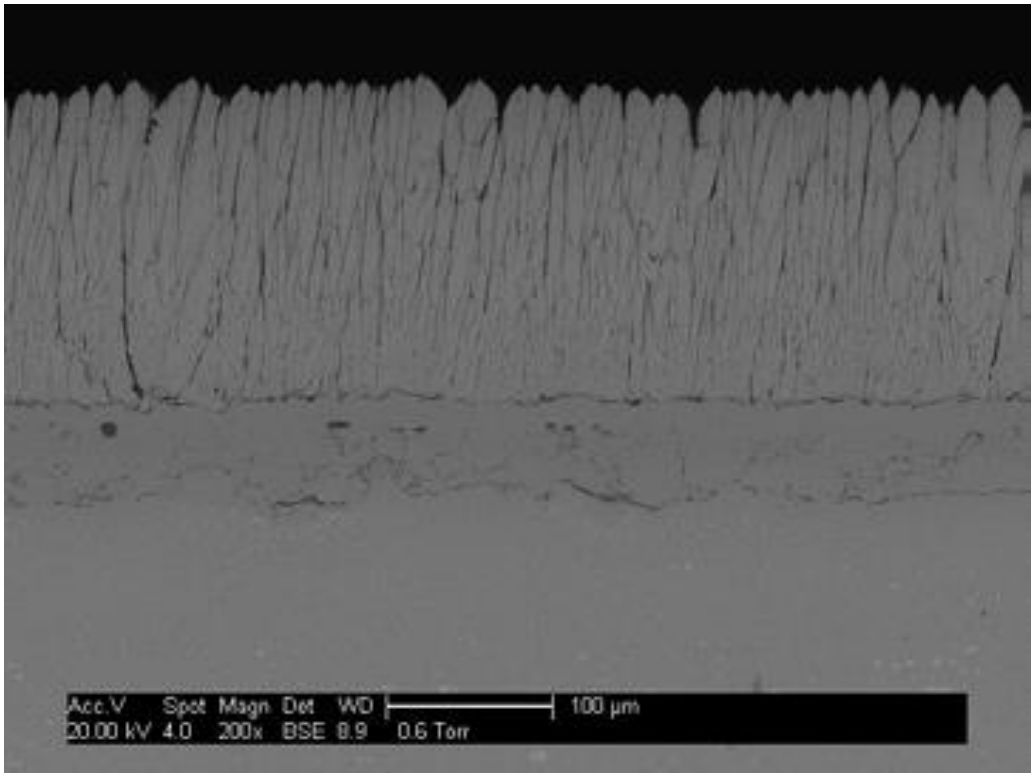

Figure 9: SEM micrograph of a TBC microstructure produced by EB-PVD.
Note the columnar microstructure [52].

To compare and investigate erosion characteristics of enamel to TBC's, the concept of the *D*/*d* ratio introduced by Wellman and Nicholls [52] is used. *D* is the contact diameter of the indenter tip and *d* is the column diameter. Wellman and Nicholls proposed that *D*/*d* ratio determines what damage mechanisms take place as shown in Figure 10.

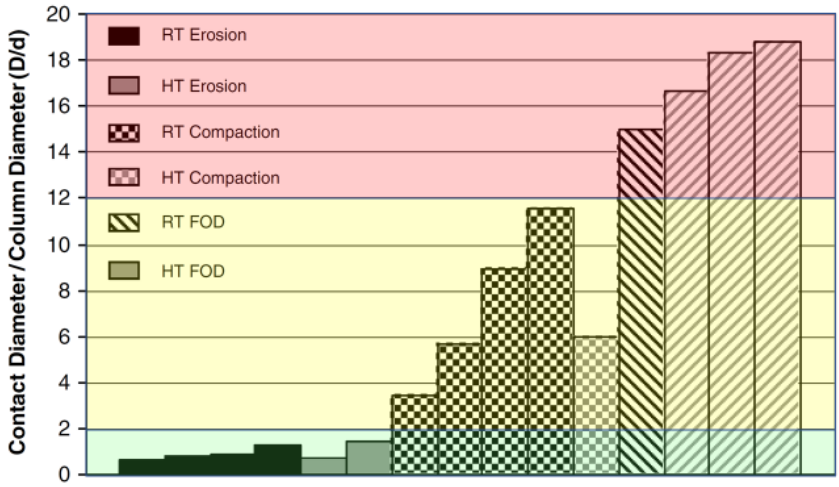

Figure 10: Plot of measured *D/d* ratios for different impact conditions, with a coloured overlay showing the different thresholds. Adapted from Wellman and Nicholls [52].

3 primary erosion mechanisms were observed:

1. Erosion (*D/d* ratio of 0-2, Green highlight)
    a. Cracking of multiple adjacent columns causes material loss.
    b. The integrity of the microstructure is unchanged.
    c. Usually for small particle impacts at the top 20μm of the surface.

2. Compaction Damage (*D/d* ratio of 2-12, Yellow highlight)
    a. A transition mechanism between erosion and FOD.
    b. Columns are compacted, without cracking from Erosion or deformation from FOD.
    c. Energy from impact spread over many columns.

3. Foreign Object Damage (FOD) (*D/d* ratio of 12-20, Red highlight)
    a. Significant deformation of the structure occurs with cracking, column deformation, gross plasticity, and shear bands observed.
    b. Caused by high velocity, small particles, or low velocity, large particles.

The *D*/*d* ratio can be supplemented Zhou's findings on tip-induced deformation of HAP crystals [18].

Chapter 4 METHODOLOGY

4.1 SAMPLE PREPARATION

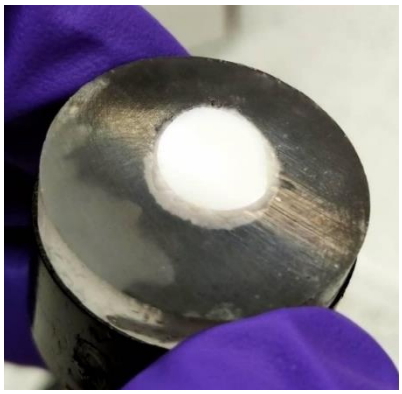

Figure 11: Bovine enamel disk glued to Bakelite block during polishing.

Sectioned and ground bovine enamel disks as shown in Figure 11 were purchased from Modus Laboratories, Reading, UK. The disks were embedded in cold cured resin (EpoFix, Struers Ltd., Catcliffe, UK). To prepare the sample for use with the nanoindenter, the working surface (the surface where enamel layer is present) must be smooth with minimal flaws and scratches as the indenter could interact with these imperfections instead of the enamel prisms, thus affecting the results obtained. With that in mind, the bovine enamel disks were sequentially polished using a 4000 grit SiC paper (Struers Ltd., Catcliffe, UK), followed by polishing with a 3µm diamond suspension on a cloth (MD-Nap, Struers Ltd., Catcliffe, UK) and finished with a 1µm diamond suspension on a cloth (MD-Nap, Struers Ltd., Catcliffe, UK)

After the polishing was complete, a rough file was used to shave away a side of the sample – an illustration is shown in Figure 12. This was done to view the sample's cross-section to ensure the enamel layer was still intact after polishing and provide a degree of orientation if subsequent tests were required on the sample.

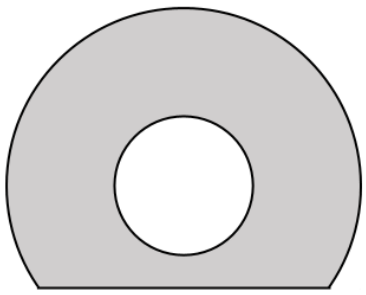

Figure 12: An illustration of the sample (top-down view) after a side was shaved away.

4.2 EXPERIMENTAL SETUP FOR NANOIMPACT AND NANOINDENTATION

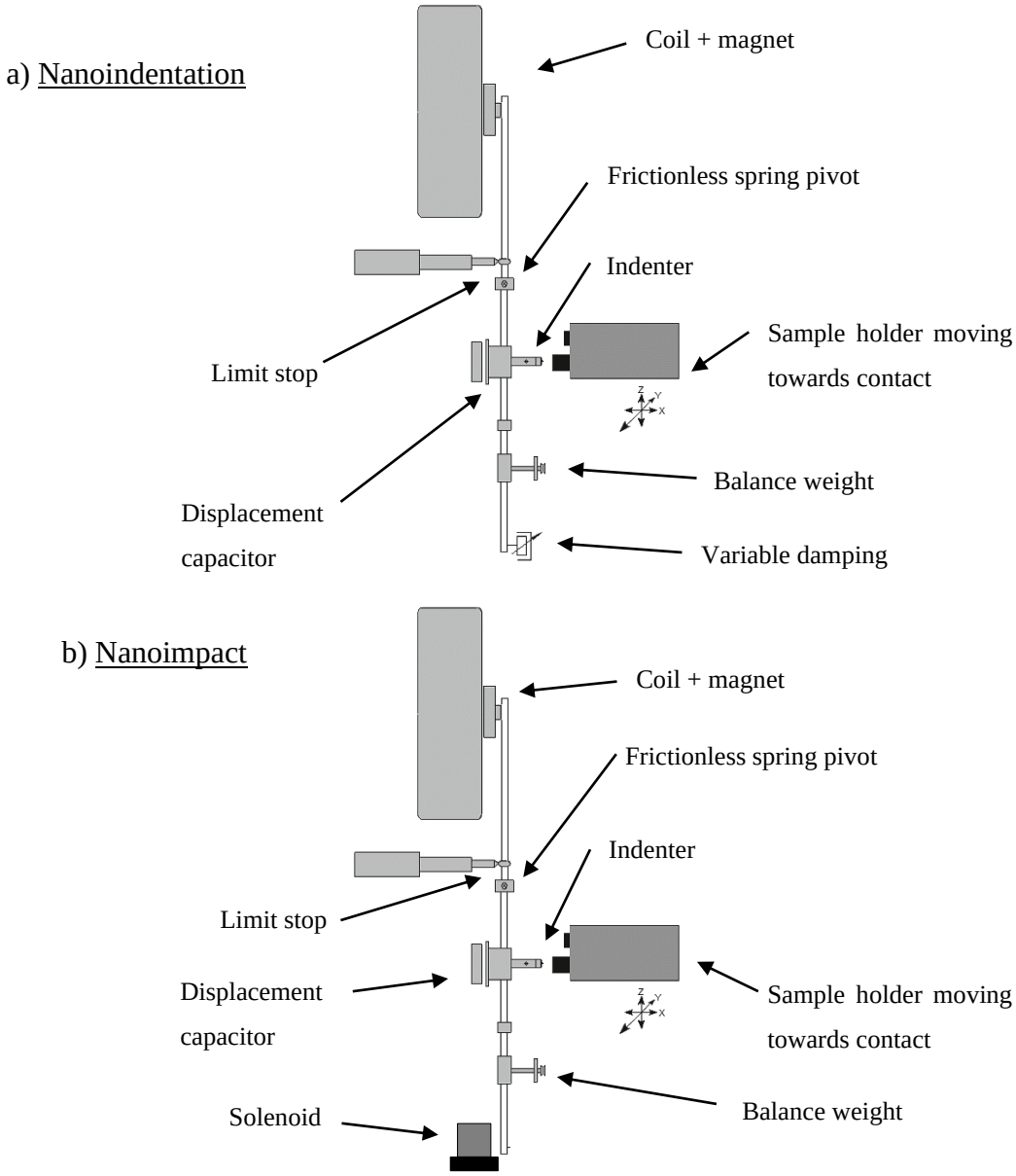

Figure 13: Schematic of nanoindentation system setups used for a) nanoindentation and b) nanoimpact tests in this experiment. Image adapted from Fischer-Scripps. [53]

Superglue was used to affix the non-working surface of the sample to the sample holder (a metal cylinder) of the NanoTest® Vantage (MicroMaterials Ltd., Wrexham, UK) [54] nanoindentation system that would perform both nanoindentation and nanoimpact testing. The setup used for the testing is shown in Figure 13.

To ensure the compliance of the sample is greater than that of the indenter, diamond was chosen as the tip material due to its high stiffness. Spherical indenters were used instead of Berkovich indenters as they are more representative of the particles used in air abrasion systems [55]. Furthermore,

spherical tips can avoid excessive damage that would result in inaccurate measurements as they reduce the stress concentrations and plastic deformation when compared to a Berkovich tip [56, 57].

A summary of the test matrix carried out is shown in Table 3. Nanoimpacts with 10 repetitions were undertaken at a load of 10mN and released at flight distances of 4, 8, 12, 16, 20, 24μm for each of the tip sizes (tip size corresponds to the radius of the sphere): 5, 10, 50, 100, 200, 500μm.

Each tip size had a different strain rate associated with it and at different flight distances, allows the strain rate of the impacts to be varied. Additionally, different tip sizes provided a range of *D/d* ratios to investigate the columnar structure effect of enamel.

The load was kept constant at 10mN to allow a fair comparison between the results and because swapping loads constantly resulted in a time-consuming setup.

For the nanoindentations, a depth-controlled indent to a maximum of 300nm was chosen for comparison purposes with the literature [12, 36, 40]. The nanoindentation setup uses a loading rate of 0.33 mN/s, unloading rate of 1.00 mN/s, dwell period at maximum load of 60 seconds, and a dwell period of 60 seconds post-indentation to account for thermal drift.

Table 3: Test matrix for nanoimpacts and nanoindents.

Type	Tip Sizes (radius of sphere in μm)	Flight Distances (μm)	Load (mN)	Number of repetitions
Nanoimpact (Constant Load)	5, 10, 50, 100, 200, 500	4, 8, 12, 16, 20, 24	10	10
Nanoindentation (Depth-Controlled)	5, 10, 50, 100, 200, 500	0.3	-	15

4.3 EXPERIMENT TRIALS WITH LIQUID CELL APPARATUS

Initial nanoimpacts and nanoindentation experiments following the test matrix shown in Table 3 were undertaken using a liquid cell apparatus as shown in Figure 14 that would completely submerge the enamel solution in distilled water. The purpose of this is to hydrate the enamel as water is required for the proteins and organic matter to function effectively [21].

However, analysis from these initial experiments showed interactions between the fluid and tip that resulted in inaccurate data. To avoid this, the entire test matrix was repeated under dry conditions, without the liquid cell apparatus, effectively carrying out the experiment and data analysis twice.

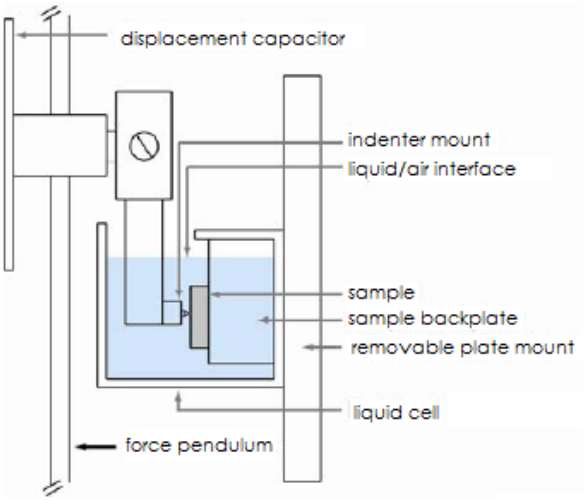

Figure 14: Diagram of liquid cell apparatus [58].

4.4 INDEPENDENT VARIABLES AND THEIR CALCULATIONS

4.4.1 STRAIN RATE

Cheng and Cheng's work suggested that the indentation strain rate (and assuming a material with power-law creep behaviour) for self-symmetric indenters, $\dot{\varepsilon}_{self\ symmetric}$, could be formulated as the ratio of the penetration rate to the current penetrated depth [59], shown below in Equation 2, where *h* is the depth penetrated

$$\dot{\varepsilon}_{self\ symmetric} = \frac{\dot{h}}{h} \qquad \text{Eq. (2)}$$

This holds true for Berkovich indenters, but not spherical indenters as it is are not self-symmetric. Tabor's equation [60, 61] is more suited to find out the indentation strain rate for spherical indenters as it allows the indentation strain to be expressed as a function of the contact radius.

Tabor's equation defined the representative indentation strain, $\varepsilon_{indentation}$, at the contact face of a spherical indenter as shown in Equation 3, where *R* is the indenter's radius and *a* is the contact radius.

$$\varepsilon_{indentation} = 0.2\left(\frac{a}{R}\right) \qquad \text{Eq. (3)}$$

The relationship between *h* and *a* is shown below in Equation 4 [62]

$$a = \sqrt{2Rh - h^2} \qquad \text{Eq. (4)}$$

As the maximum indentation strain was required to give a better representative value of the strain rate, maximum depth, h_{max}, was used and Equation 4 is now changed to Equation 5

$$a = \sqrt{2Rh_{max} - {h_{max}}^2} \qquad \text{Eq. (5)}$$

All parameters combined, the representative indentation strain of the spherical indenter is shown in Equation 6 as a function of the maximum depth penetrated.

$$\varepsilon_{indentation} = 0.2\left(\frac{\sqrt{2Rh_{max} - {h_{max}}^2}}{R}\right) \quad \text{Eq. (6)}$$

Calculating the indentation strain rate for spherical indenters, $\dot{\varepsilon}$, is then just a simple matter of numerical differentiation [62] of the strain value against time as shown in Equation 7

$$\dot{\varepsilon} = \frac{d\varepsilon_{indentation}}{dt} \quad \text{Eq. (7)}$$

The depth-time data exported from the MicroMaterials Control software is manipulated in Microsoft Excel for calculation of the strain rates from nanoimpacts while strain rates from nanoindentations are exported directly.

4.4.2 D/D RATIO

The dimensionless erosion ratio, *D/d*, was introduced by Wellman [52] in his work on the erosion of TBC's to relate different erosion mechanisms to the size of the impact.

$$\frac{\mathrm{D}}{\mathrm{d}}\ \text{ratio} = \frac{\text{contact footprint diameter}}{\text{column diameter}} \quad \text{Eq. (8)}$$

The contact footprint diameter, *D*, is simply Equation 5 multiplied by 2.

$$D = 2\sqrt{2Rh_{max} - {h_{max}}^2} \quad \text{Eq. (9)}$$

The column diameter, *d*, for bovine enamel prisms are assumed to be an average value of 6μm [23]. Effectively, the *D/d* ratio is also equal to the number of columns that the indenter interacts with.

The *D/d* ratio is useful at it incorporates many variables that are difficult to resolve such as particle size and particle velocity. It was used to determine erosion regimes for TBCs as mentioned in Chapter 3.7. [52]

4.5 DEPENDENT VARIABLES AND THEIR CALCULATIONS

4.5.1 DYNAMIC HARDNESS

The dynamic hardness, *DH*, (quantified in GPa) is defined as the ratio of the energy consumed during an impact to the volume of material displaced by said indentation [53, 63, 64]. The equation to calculate dynamic hardness as used by Wheeler and Gunner [64] is shown below in Equation 10.

$$h_{dyn} = \frac{\frac{1}{2} m_{eff}(v_{in} - v_{out})}{\int_0^{h_{rest}} f_{SAF}(h)} \quad \text{Eq. (10)}$$

Where m_{eff} is the effective pendulum mass, v is the velocity, h_{rest} is the depth where the pendulum comes to rest and f_{SAF} is the spherical area function of the indenter.

The equation for calculating f_{SAF} using a second-order polynomial is shown in Equation 11 [65]. A second-order polynomial is used because the MicroMaterials control software uses this polynomial for the ideal area function of a sphere.

$$f_{SAF}(h) = A + Bh + Ch^2 \quad \text{Eq. (11)}$$

The values of coefficients A, B, and C are different for spheres with different radiuses. To obtain the coefficients: a multi-point analysis of the spherical area function was carried out with the MicroMaterials control software to produce a plot of the projected contact area vs the contact depth. As the software does not allow direct export of this plot, 50 datapoints were selected by hand and then replotted in SigmaPlot (Systat Software Inc., Berkshire, UK). A polynomial curve was fitted to the datapoints to produce the coefficient values. This was repeated for all 6 tip sizes, with the values summarized in Table 4 below.

Table 4: Coefficients for ideal area function of spheres with radius 5μm-500μm.

Coefficient	Tip radius (μm)					
	5	10	50	100	200	500
A	-26115.9	-135578.2	-15025255.708779	-22278979.585429	-144393219.38	-689477879.82
B	31393.0	62899.4	314739.7827	628305.4151	1256777.96	3134864.20
C	-3.134	-3.1540	-3.1426	-3.1438	-3.1459	-3.1239

4.5.2 COEFFICIENT OF RESTITUTION

The coefficient of restitution, *CoR*, is defined as the ratio of the velocity of separation to the velocity of approach for a collision between two bodies [66].

In Equation # below, u_1 and u_2 represent the velocities of the bodies before collision while v_2 and v_1 represent the velocities of the bodies after collision [67].

$$\text{CoR} = \left|\frac{v_2 - v_1}{u_2 - u_1}\right| \quad \text{Eq. (12)}$$

CoR always takes a value between 0 and 1, with e = 1 indicating a perfectly elastic collision where no kinetic energy is dissipated.

As the sample is stationary in the nanoimpact setup, the equation [67] simplifies to

$$\text{CoR} = \left|\frac{v_{out,\ indenter}}{v_{in,\ indenter}}\right| \qquad \text{Eq. (13)}$$

4.5.3 IMPACT ENERGY

The energy transfer per impact, E_{impact}, was quantified in nanojoules (nJ) using Equation 14 below proposed by Beake et al [68].

$$E_{impact} = \text{Force} \times P\text{endulum Swing Distance} \qquad \text{Eq. (14)}$$

Since maximum impact energy was to be determined, the calculations in this report used the maximum depth, h_{max} , penetrated by the indenter, as shown in Equation 15

$$E_{impact} = \text{Force of indenter} \times h_{max} \qquad \text{Eq. (15)}$$

4.5.4 DYNAMIC DEPTH

The dynamic depth (quantified in μm) of an indentation is the maximum penetration depth minus the rest depth when the pendulum comes to a complete rest. The equation to calculate dynamic depth as used by Wheeler and Gunner [64] is shown below in Equation 16.

$$h_{dyn} = h_{max} - h_{rest} \qquad \text{Eq. (16)}$$

4.5.5 STRAIN RATE SENSITIVITY

SRS is by parameter *m*. *m* can be calculated from the power-law relationship as used by Maier-Kiener and Durst [48] that links strain rate, $\dot{\varepsilon}$ to plastic stress, σ, as shown in Equation 17.

$$\sigma = \dot{\varepsilon}^m \qquad \text{Eq. (17)}$$

In nanoindentation, the indentation stress is used instead. Indentation stress can also be represented by the hardness, H. After rearranging to make *m* the subject, Equation 18 below shows how to calculate SRS.

$$m = \frac{ln\ H}{ln\ \dot{\varepsilon}} \qquad \text{Eq. (18)}$$

4.6 STATISTICAL ANALYSIS

All data were expressed as the mean ± standard deviation except where specified. This data was statistically analysed using a 1-way analysis of variance (ANOVA) test in SigmaPlot (Systat Software Inc., Berkshire, UK), and differences with a p-value of <0.05 deemed as statistically significant.

Bell curves shown in Figures 15,16,17,18, were plotted to show the distribution of the measured variables and ease the process of filtering outliers in the data. Outliers here are defined as data deviating from more than 2 standard deviations of the mean, indicated by a vertical, dashed threshold line.

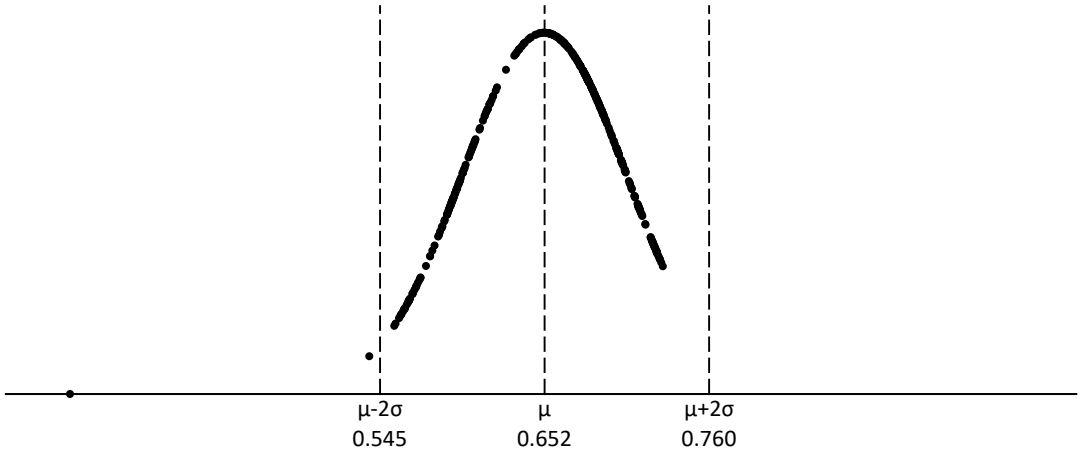

Figure 15: Normal distribution for coefficient of restitution values obtained.

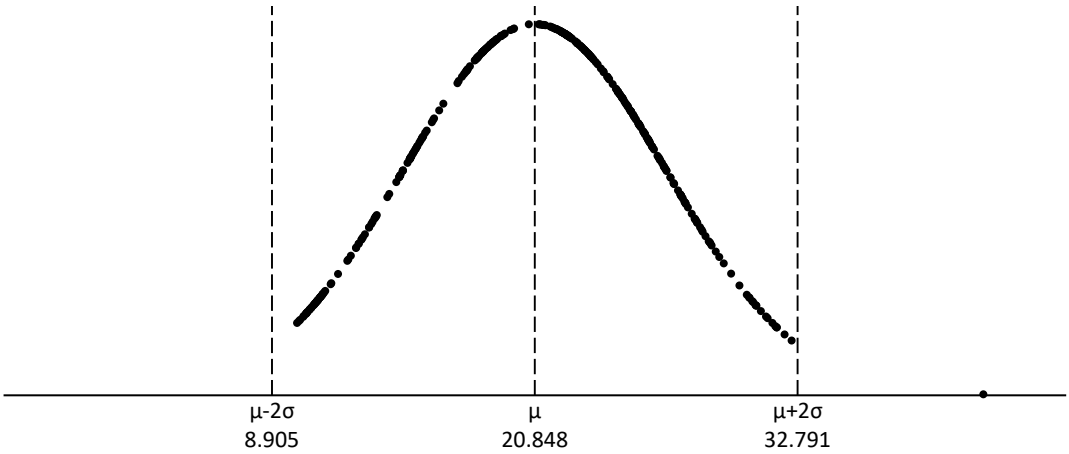

Figure 16: Normal distribution for impact energy values obtained.

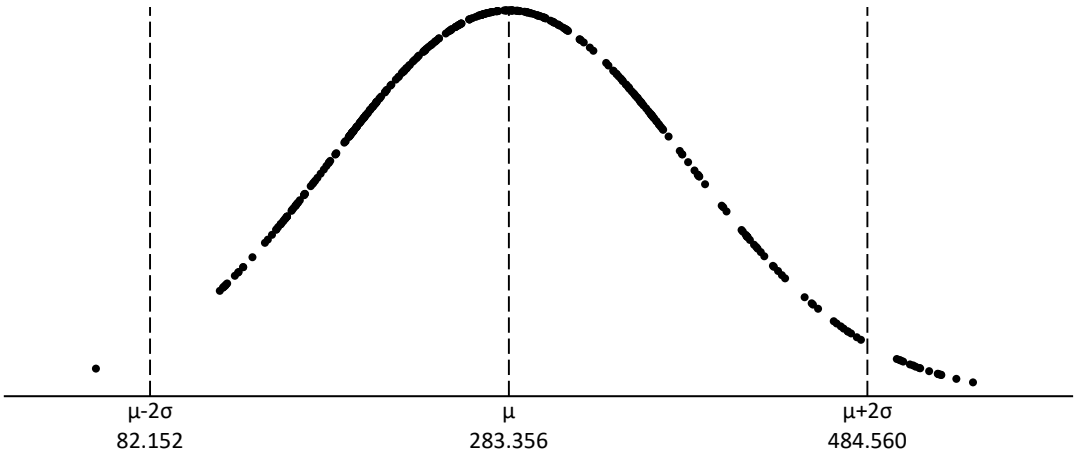

Figure 17: Normal distribution for dynamic depth values obtained.

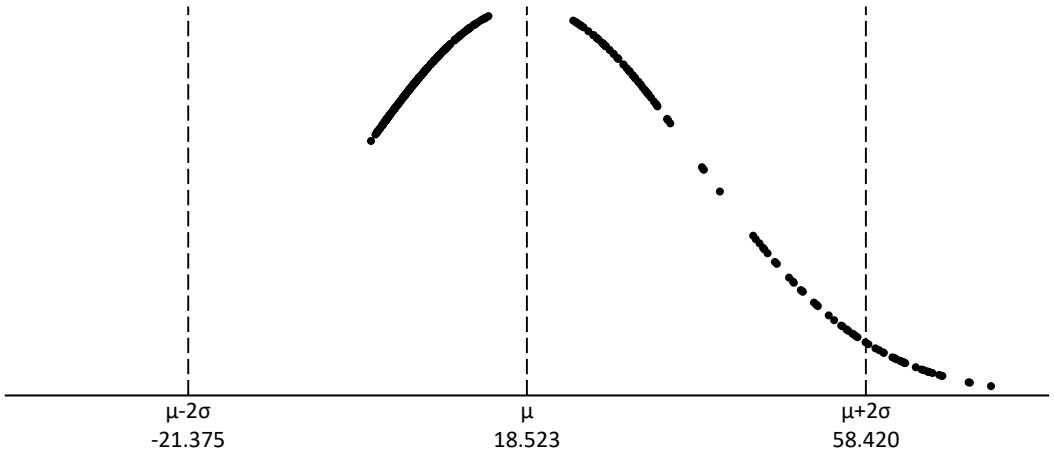

Figure 18: Normal distribution for dynamic hardness values obtained.

Moreover, multiple regression analysis was carried out using *D/d* ratio and strain rate as predictors to estimate the values of the Dependent Variables. The outcome of this analysis is shown in Appendix A.

4.6.1 DEALING WITH OUTLIERS.

In Figure 15 and Figure 16 for the *CoR* and Impact energy values respectively, discrete outliers can be seen beyond the μ ± 2σ threshold line at the left and right of the plot.

However, in Figure 17 and Figure 18 for dynamic depth and dynamic hardness values respectively, it appears that a sizeable number of datapoints cross the threshold line of 2 standard deviations of the mean.

For dynamic depth values, a total of 24 datapoints were found lying beyond 2 standard deviations of the mean (see Figure 17). However, 10 of these datapoints were from the nanoimpact test using the 10μm tip at a flight distance of 24μm and 7 of these datapoints from the nanoimpact test using the

10µm tip at a flight distance of 20µm. These 17 points were not excluded and kept in the results to better represent the data obtained overall, as removing these 17 points would effectively 'drop' a set of impacts that have been carried out. The remaining 7 outliers were discarded, and visualization of these outliers can be seen in Figure 19.

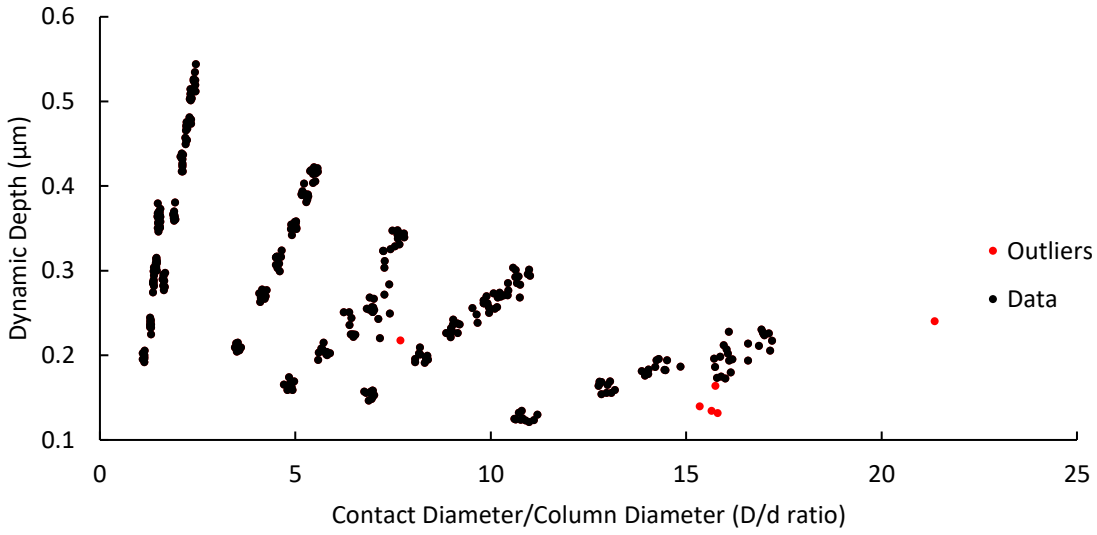

Figure 19: Scatter plot of dynamic depth vs *D/d* to visualize outliers.

For the dynamic hardness values, a total of 29 datapoints were found lying beyond 2 standard deviations of the mean (see Figure 18). Of these 29 datapoints, 25 of them are from the 5µm tip, which suggests that the 5µm tip has 'noisy' data with a large distribution. The remaining 4 outliers, and a visualization of these outliers can be seen in Figure 20.

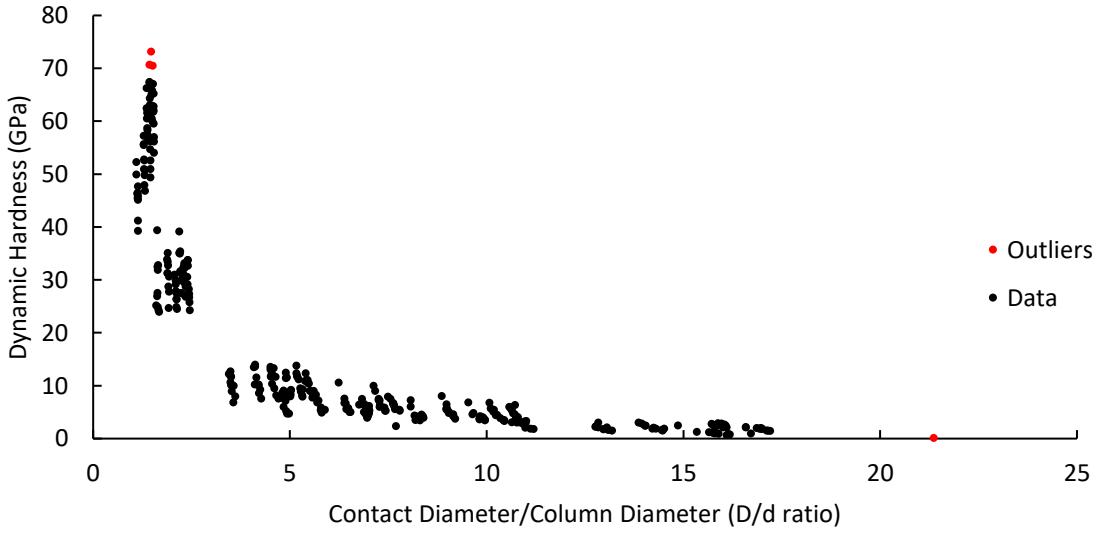

Figure 20: Plot of dynamic hardness vs *D/d* ratio to visualize outliers.

Additionally, one repetition from the test matrix was not used in the calculations for *CoR* as it was erroneous and did not fit the trend of the 9 other repetitions of the test. This repetition belonged to

the dataset for nanoimpact of the 500µm tip at a flight distance of 16µm. Figure 21 visually shows the noticeable deviation of this impact compared to the other repetitions.

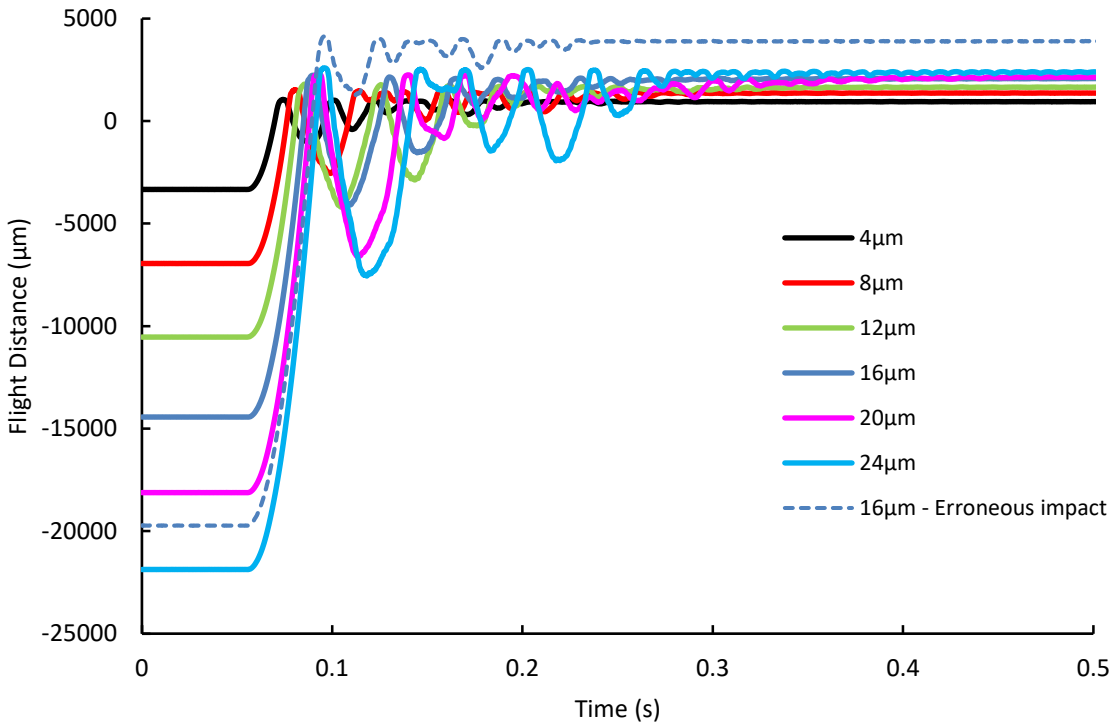

Figure 21: Depth-Time plot for nanoimpact test using 500um tip at flight distances of 4, 8, 12, 16, 20, 24µm. The erroneous data is shown with a blue dotted line.

Note: Even though the indenter tip is not released at exactly 4/8/12/16/20/24µm as can be seen in Figure 21, the velocities are changed and this change is integrated into the distribution of the strain rate, *D/d* ratio and other unified values extracted from the data. The release point is also within 1µm for each flight distance. This small difference is not significant as it is dealt with through the analysis of the data.

Chapter 5 RESULTS

Note: Strain rate and *D/d* ratio are linked to the size of the tip used. A small tip has a larger strain rate effect compared to a large tip, while a large tip has a higher *D/d* ratio compared to a small tip. Error bars represent 1 standard deviation.

5.1 PLOTS FOR STRAIN RATE

5.1.1 DYNAMIC HARDNESS VS STRAIN RATE

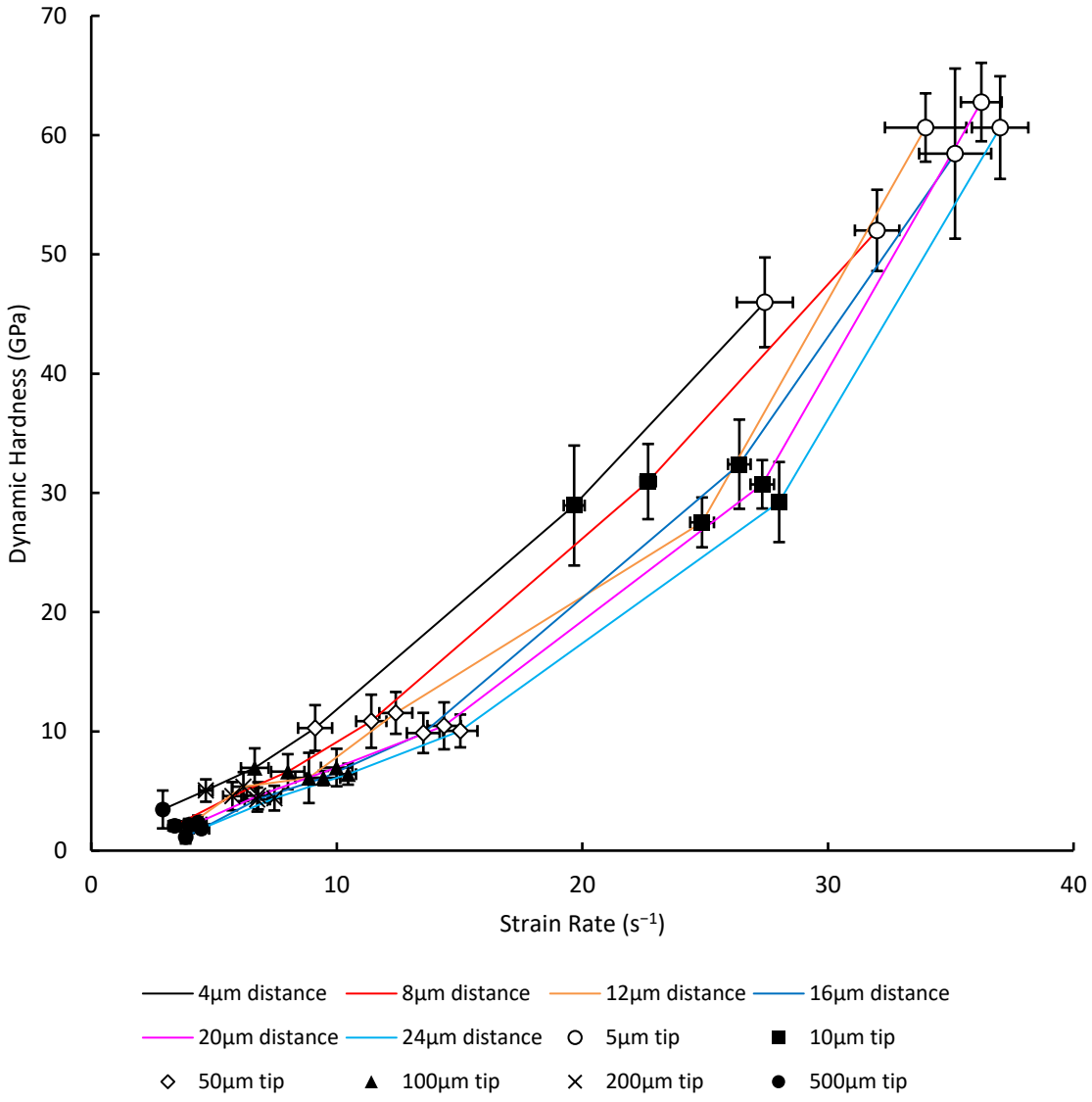

Figure 22: Plot of dynamic hardness vs strain rate

The plot of dynamic hardness vs strain rate in Figure 22 shows a trend of increasing dynamic hardness with strain rate. Within a tip, the dynamic hardness values are more spread out at different flight distances as the tip size is increased from 5μm to 500 μm.

There is a noticeable difference between the dynamic hardness values obtained by the larger tips (50,100,200,500μm) and the smaller tips (5 and 10μm). The average dynamic hardness value across all flight distances for the 5μm tip and 10μm tip is 56.74 GPa and 29.96 GPa respectively while for the 50,100,200,500μm tips combined it is 5.98 GPa. This is an approximate difference of nearly 4-8.5 times in value of dynamic hardness between the smaller tips and the larger tips. Average dynamic hardness values across all flight distances by each tip size are shown in Table 5.

Table 5: Average dynamic hardness (GPa) values for each tip size.

Classification	Tip size (μm)	Average dynamic hardness (GPa)	
Smaller Tips	5	56.74327	
	10	29.96033	
Large Tips	50	10.50975	5.976674 (average of large tips)
	100	6.519206	
	200	4.710058	
	500	2.16768	

A best-fit analysis was conducted using Microsoft Excel to determine the effects of smaller and larger tips on dynamic hardness. Linear fits were plotted through all the tips, then excluding the 5μm tip, followed by excluding both the 5μm and 10μm tip as shown in Figure 23. The R^2 values are compiled in Table 6.

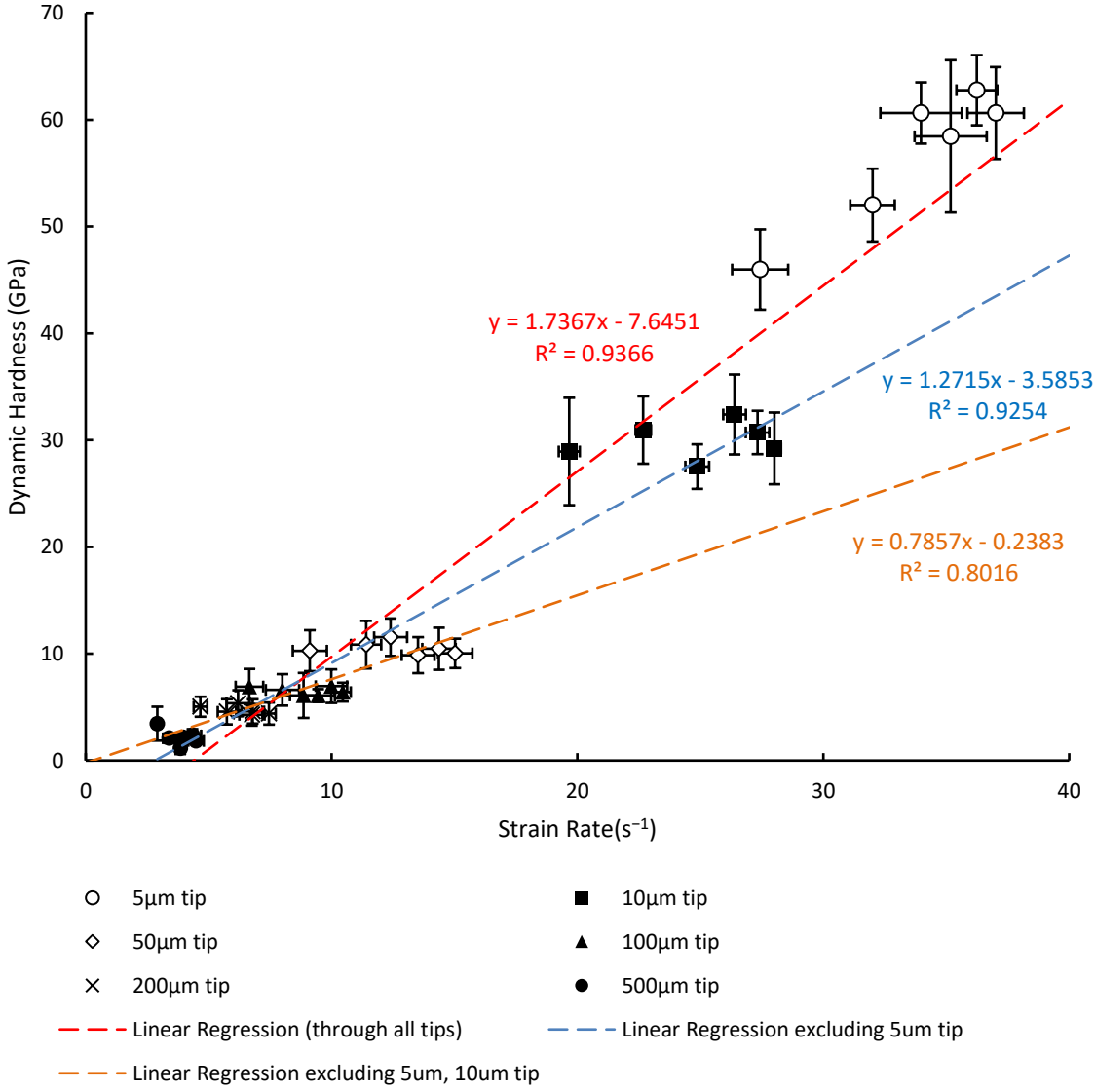

Figure 23: Plot of dynamic hardness vs strain rate. Best-fit lines added to view the relationship between tip sizes and effect on dynamic hardness value.

Table 6: R^2 values and linear equations for regression lines in Figure 23.

Classification	Tip Sizes used (µm)	R^2 value of Linear Fit	Linear Equation
All tips	5,10,50,100,200,500	0.9366	y = 1.7367x - 7.6451
Excluding 5µm tip	10,50,100,200,500	0.9254	y = 1.2715x - 3.5853
Large Tips only	50,100,200,500	0.8016	y = 0.7857x - 0.2383

Looking at the gradients of the linear equation, the smaller tips give a larger change in dynamic hardness values as indicated by a bigger gradient in the linear equation.

5.1.2 IMPACT ENERGY VS STRAIN RATE

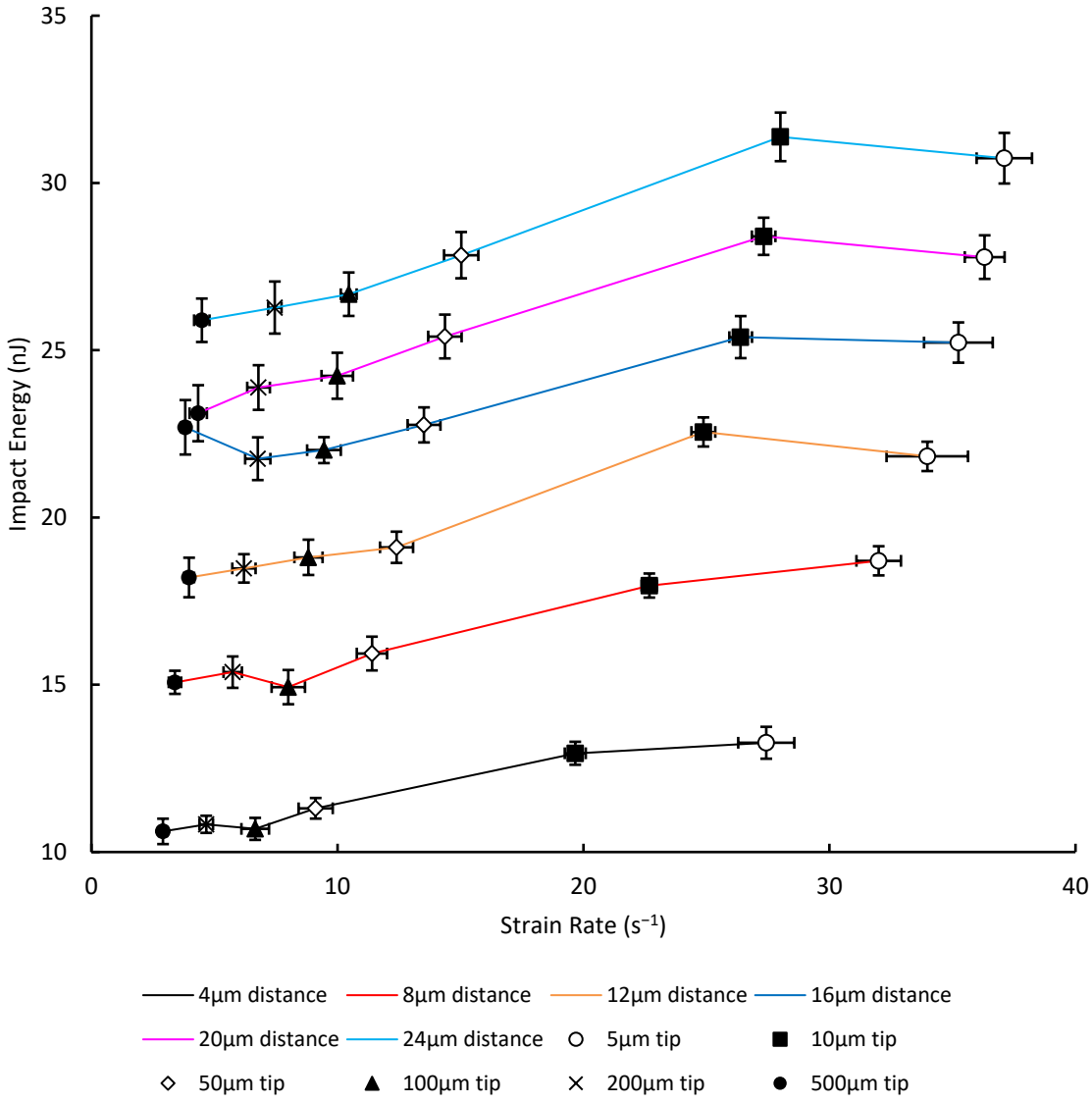

Figure 24: Plot of Impact energy vs strain rate

The plot of Impact energy vs strain rate as shown in Figure 22 shows the Impact energy increasing nearly linearly with strain rate for the 4µm and 8µm flight distances. However, the remaining flight distances show the Impact energy increasing up until the 10µm tip then dropping slightly when the 5µm tip is used; indicating a point of inflexion between the 5µm and 10µm tip.

When looking within a specific tip, the impact energies increase with a higher flight distance. Additionally, within a tip, the strain rate also increases as the flight distance is increased but to a lesser extent compared to when the tip size is decreased.

5.1.3 Dynamic Depth vs Strain Rate

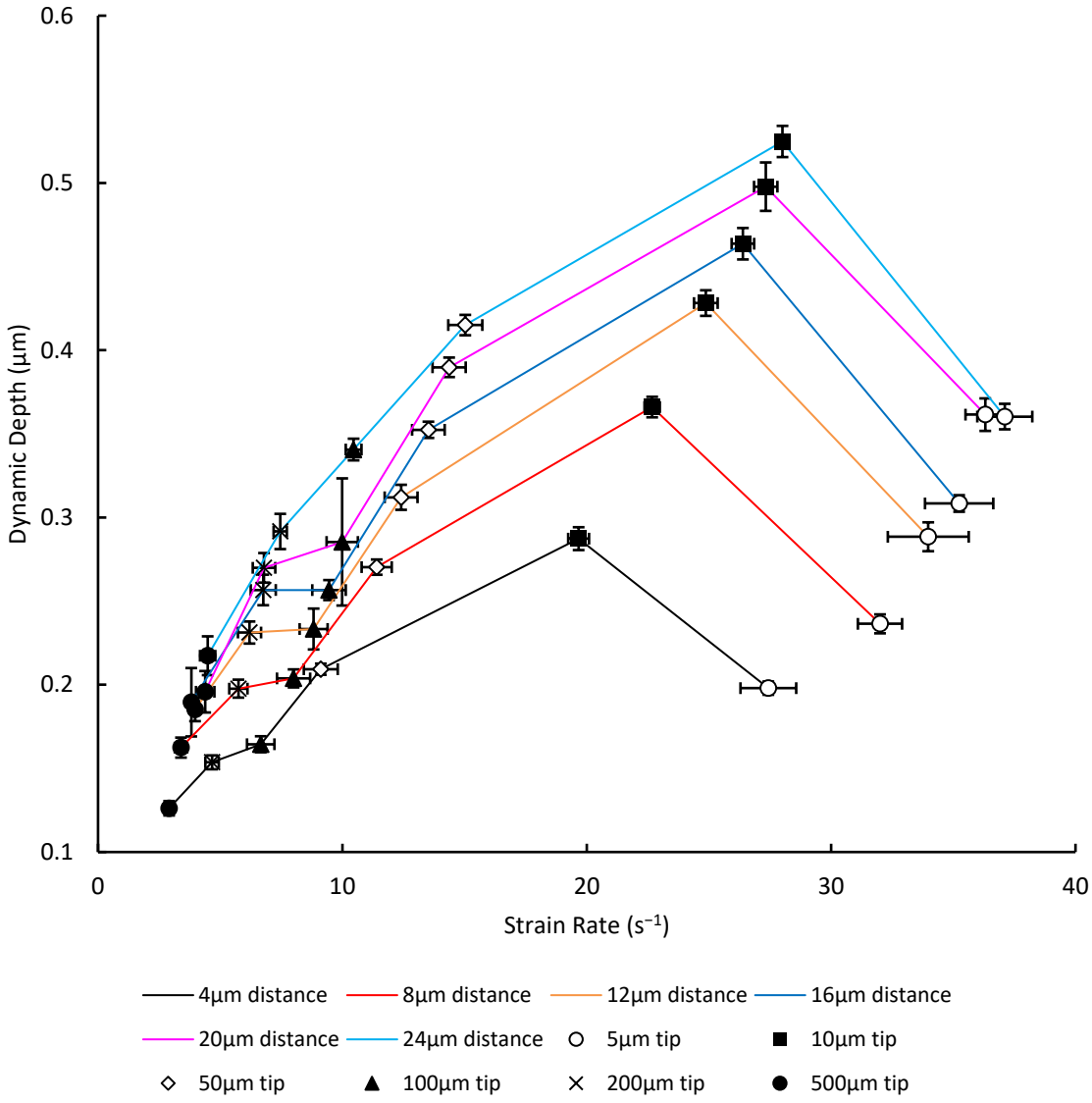

Figure 25: Plot of dynamic depth vs strain rate

The plot of dynamic depth vs strain rate as shown in Figure 25 shows the dynamic depth increasing almost linearly with strain rate as the tip sizes decrease, until the 10µm tip. There is a point of inflexion here as the 5µm tip drops to a lower dynamic depth compared to the 10µm tip.

When looking within a specific tip, the dynamic depth increases as the flight distance increases.

5.1.4 Coefficient of Restitution vs Strain Rate

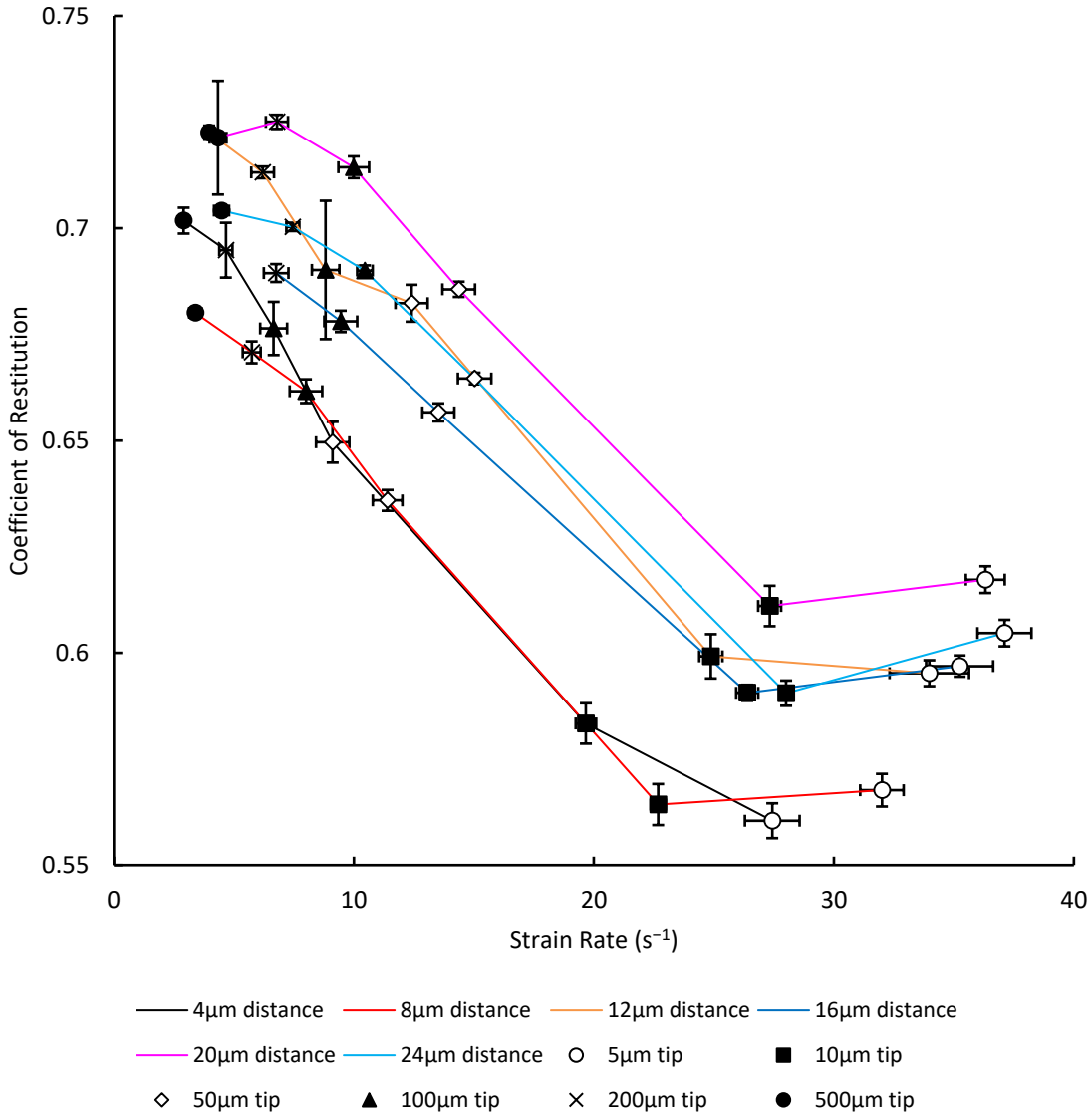

Figure 26: Plot of coefficient of restitution vs strain rate

The plot of *CoR* vs strain rate as shown in Figure 26 shows the trend that the *CoR* is decreasing with increasing strain rate to a minimum up to the 10µm tip then increases again when the 5µm tip is used. This represents another point of inflexion between the two smallest tips as the *CoR* for the 5µm tip is slightly higher than that of the 10µm tip.

There is some overlap with the 4,8µm flight distance, and the 12,24µm flight distance. Within a tip, the 20µm flight distance provides the highest *CoR* values for all tip sizes.

5.2 PLOTS FOR D/D RATIO

5.2.1 DYNAMIC HARDNESS VS D/D RATIO

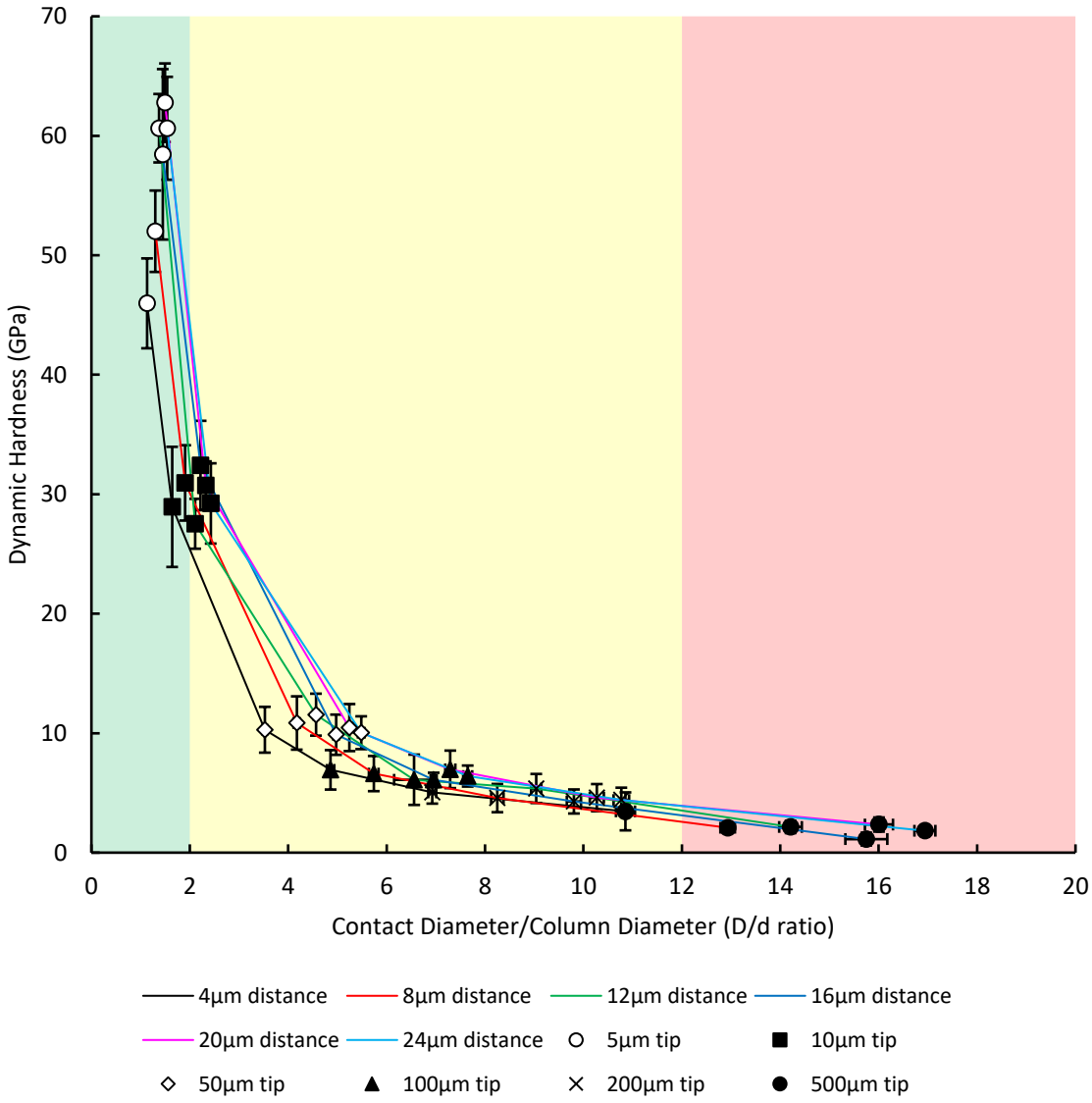

Figure 27: Plot of dynamic hardness vs *D/d* ratio

The plot of dynamic hardness vs *D/d* ratio shows dynamic hardness decreasing as the *D/d* ratio increases. Looking within a tip, the spread of data goes from a big spread of dynamic hardness values and a small spread of *D/d* ratios to the opposite, as the size of tip increases from 5µm to 500µm.

The smaller tips have a *D/d* ratio on average no higher than 2 while the larger tips have a *D/d* ratio of 3+.

Best-fit analysis was done on this plot using a negative exponential fit. One line of best fit was tested using data points from all the tips, while another line of best fit used only data points from the larger tips. The lines of best fit are shown in Figure 28 and R^2 values in Table 7.

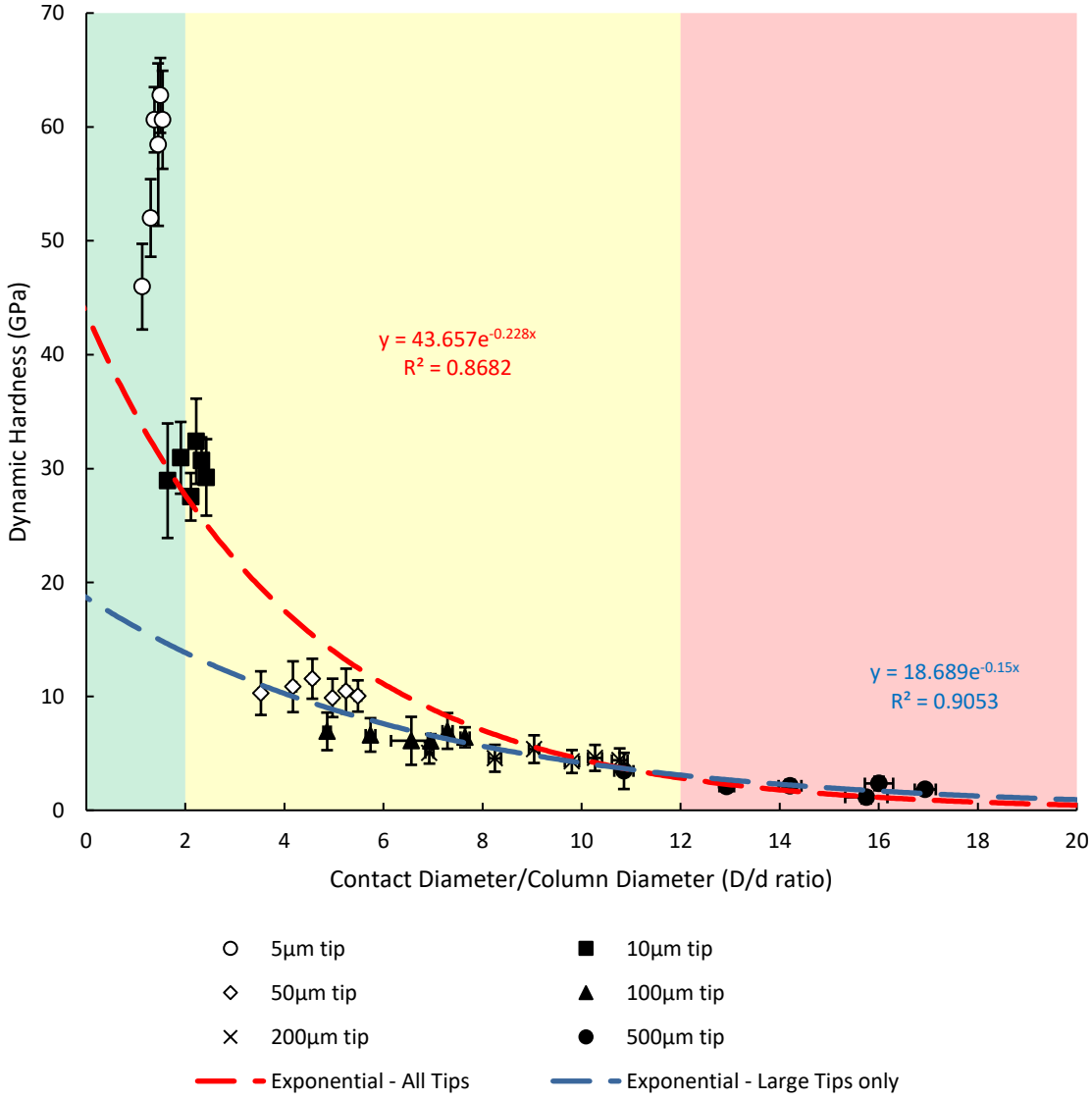

Figure 28: Plot of dynamic hardness vs *D/d* ratio. Best-fit lines added to view the relationship between tip sizes and effect on dynamic hardness value.

Table 7: R^2 values and negative exponential equations for regression lines in Figure 28.

Classification	Tip Sizes used (µm)	R^2 value of Negative Exponential Fit	Negative Exponential Equation
All Tips	5,10,50,100,200,500	0.8682	$y = 43.657e^{-0.228x}$
Large Tips only	50,100,200,500	0.9053	$y = 18.689e^{-0.15x}$

The best fit analysis shows that the smaller 5µm tip and 10µm tip behave differently compared to the larger as they result in higher dynamic hardness values, and do not follow the line of best fit that goes through the larger tips.

5.2.2 IMPACT ENERGY VS D/D RATIO

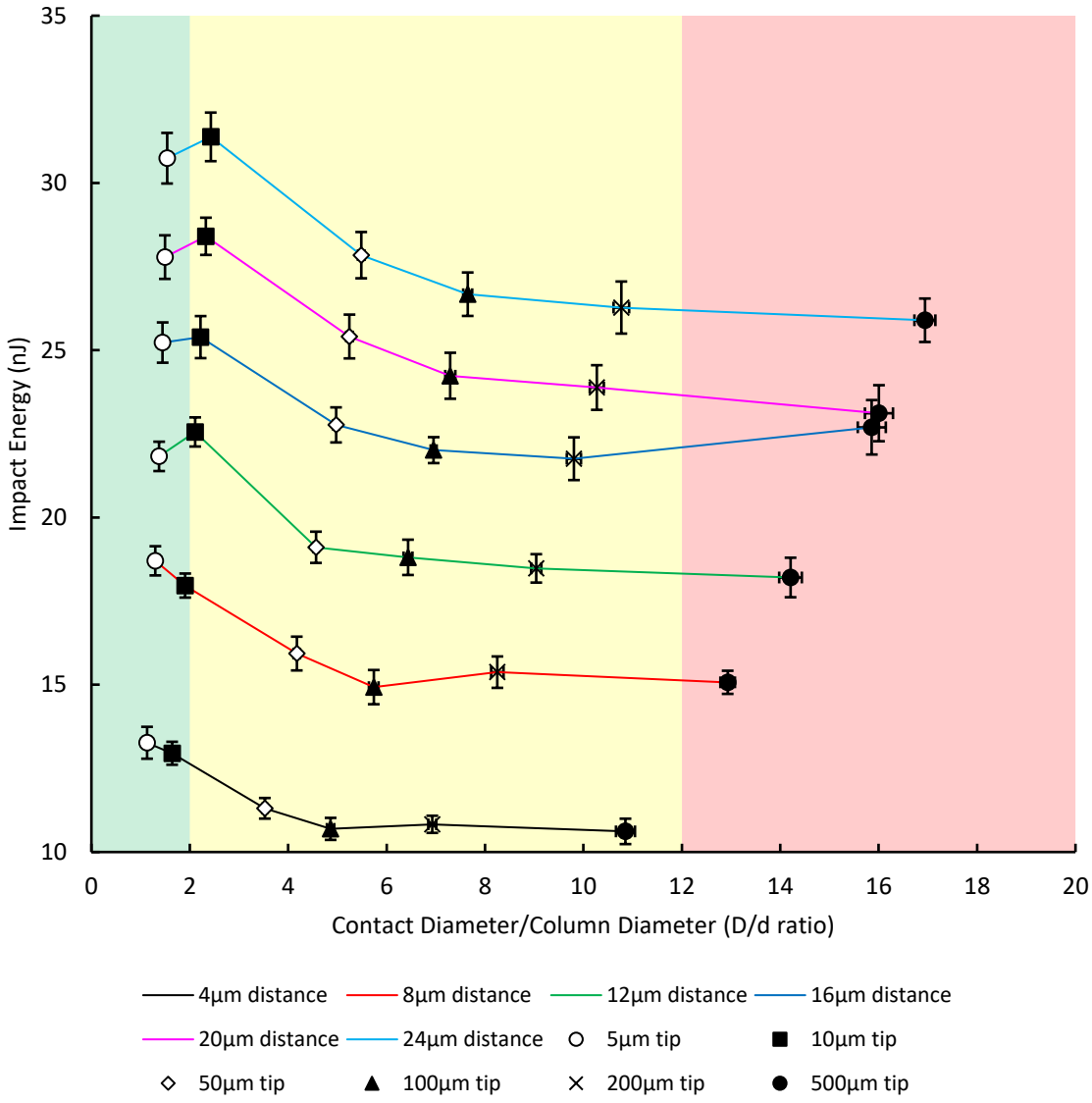

Figure 29: Plot of Impact energy vs *D/d* ratio

The plot of Impact energy vs *D/d* ratio shown in Figure 28 shows the Impact energy decreasing with higher *D/d* ratios. Within a single tip, the impact energies increased steadily with increasing flight distance. The size of the tips seems to influence the impact energy as the larger tips e.g 500µm tip has a more dramatic *D/d* change compared to the smaller tip e.g 5µm tip.

An interesting observation is seen with the 10µm tip. At 4µm and 8µm flight distances, the 10µm tip has a *D/d* ratio of 2, and results in a smaller impact energy than the 5µm tip. However, at longer flight distances, the 10µm tip has a *D/d* ratio above 2 and achieves an impact energy greater than the 5µm tip did. This alludes to the fact that there is a different structural effect taking place below *D/d* ratios of 2.

5.2.3 Dynamic Depth vs D/d ratio

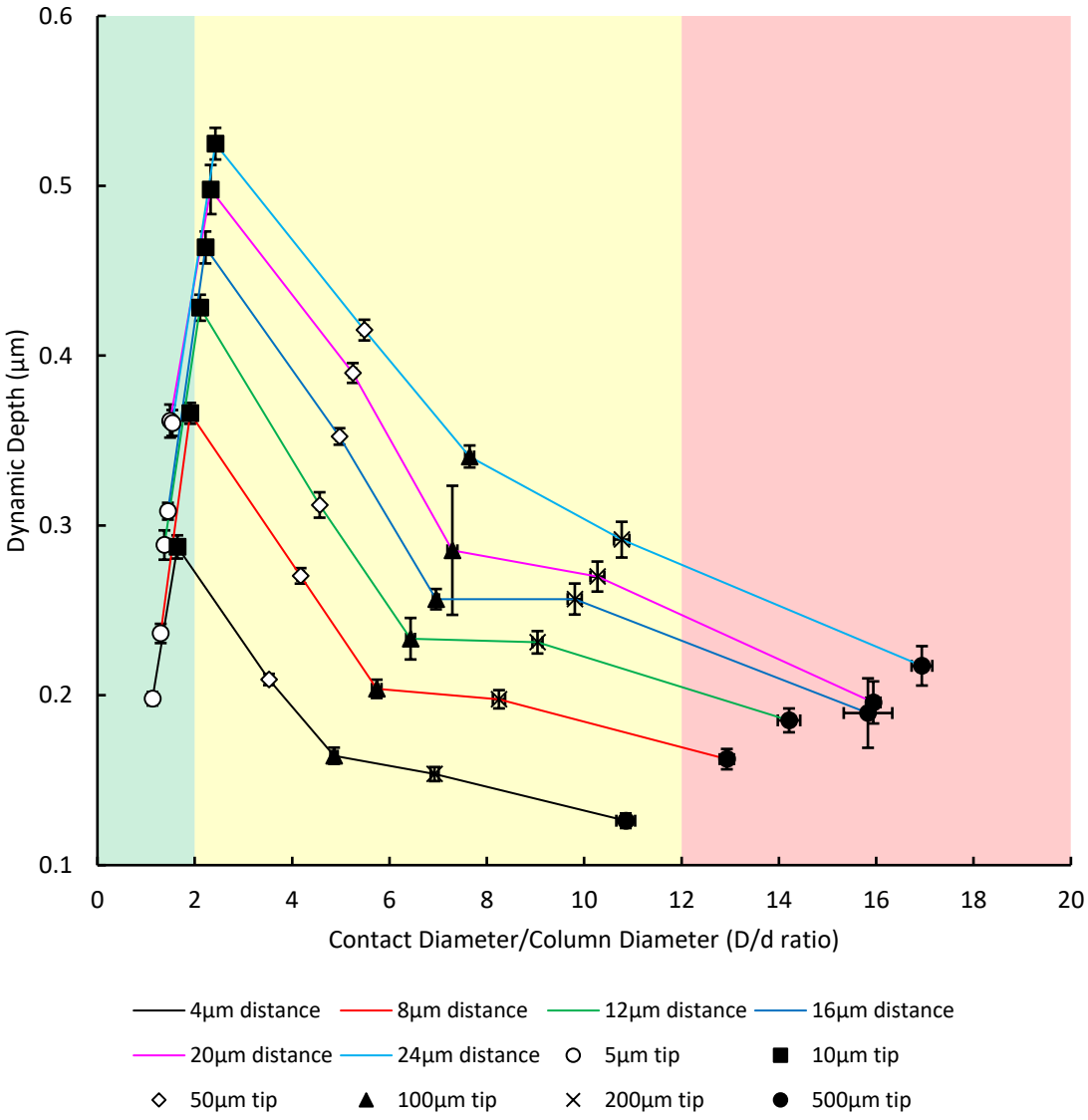

Figure 30: Plot of dynamic depth vs *D/d* ratio

The plot of dynamic depth vs *D/d* ratio shown in Figure 30 shows a clear trend that the dynamic depth decreases with increasing *D/d* ratio for the 10um tip till the 500um tip. The 5um tip has a considerably lower dynamic depth value than the 10um tip, pointing to a point of inflexion here due to structural effect. The 5um tip impact is also below a *D/d* ratio of 2 while the 10um tip is above a *D/d* ratio of 2 when the flight distances have been averaged.

Within a tip, the dynamic depth increases as the flight distances are increased. The larger sized tips show a greater *D/d* change compared to the smaller sized tips.

5.2.4 COEFFICIENT OF RESTITUTION VS D/D RATIO

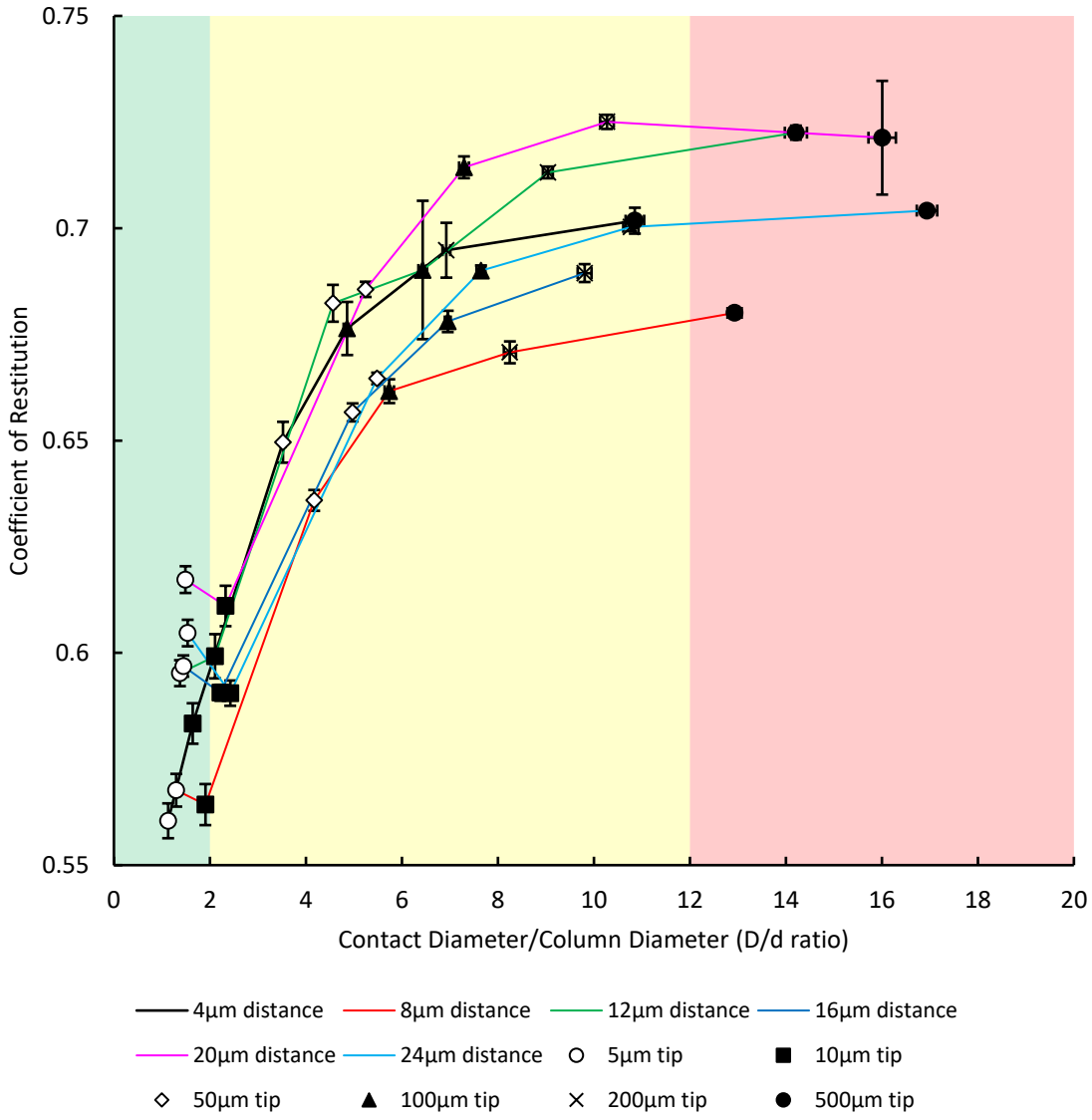

Figure 31: Plot of *CoR* vs *D/d* ratio

The plot of *CoR* vs *D/d* ratio as shown in Figure 26 shows the *CoR* is increasing with increasing *D/d* ratios.

The 5um tip shows a larger *CoR* compared to the 10um tip and does not fit the overall trend, and represents another point of inflexion between the two tips possibly due to structure effect.

The large 500um tip shows a greater *D/d* change compared to the smaller 5um tip. The *CoR* values appear to level off as the *D/d* ratio increases from 2 - 20, suggesting a structure effect here as well. Most of the variability in the *CoR* values occurs between *D/d* ratio 2 - 12.

5.3 COMBINED PLOTS FOR STRAIN RATE AND D/D RATIO

The plots below show the same data from Chapter 5.1 and 5.2, but with strain rate and *D/d* ratio combined to ease viewing the relationship between dependent variables, strain rate and *D/d* ratio (number of columns impacted). Only the average of the data from all flight distances were used and error bars were removed to prevent cluttering.

In all 4 plots below, the relationship between values of the dependent variables and strain rates are strong linear relationships ($R^2 > 0.95$) except for the 5μm tip which does not fall near the line. Adding to this observation, the 5μm tip is shown to hit less than 2 columns while the other tips hit 2-14 columns.

5.3.1 Dynamic Hardness – Combined Plot

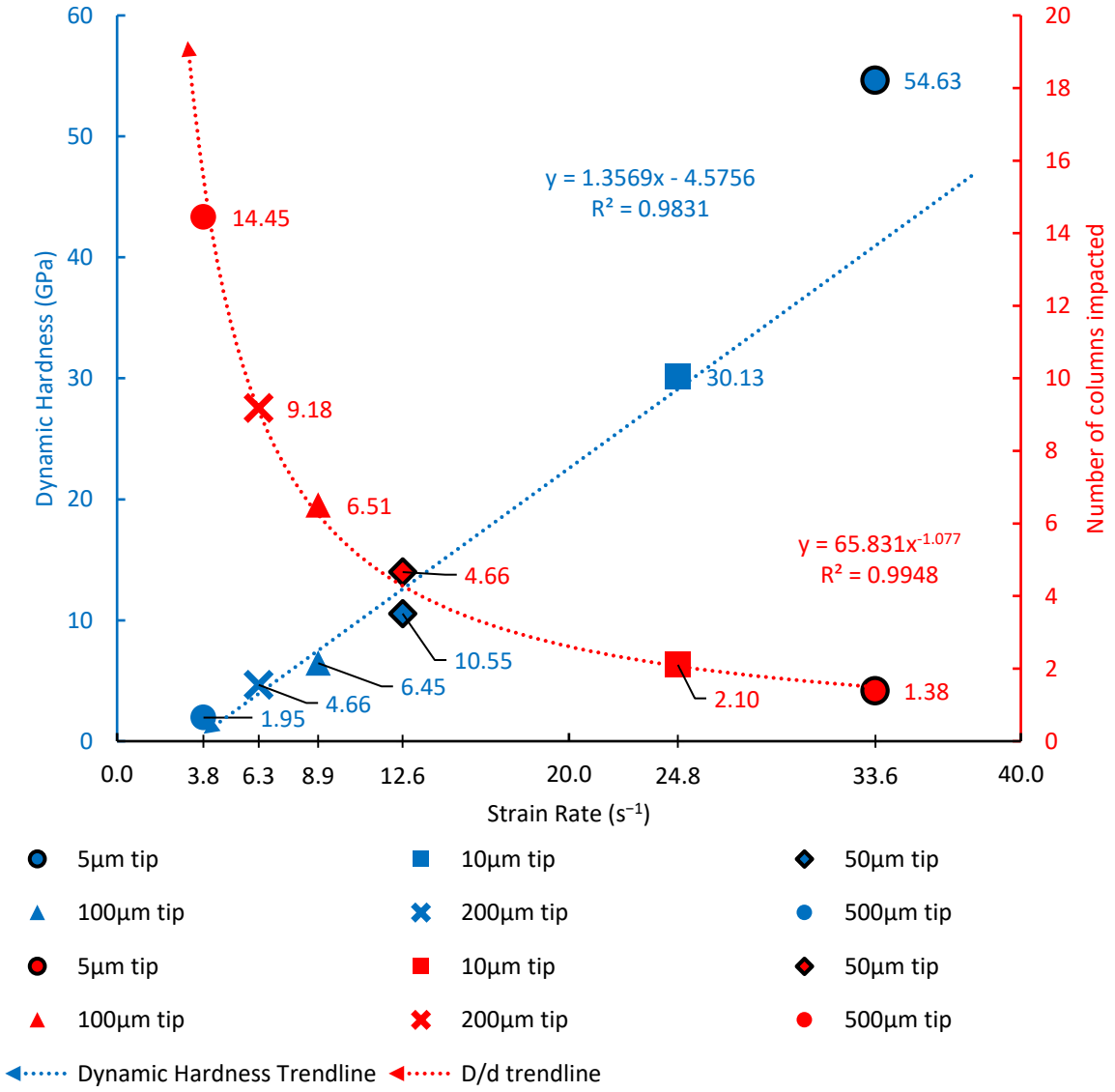

Figure 32: Combined plot showing the relationship between strain rate and *D/d* ratio on dynamic hardness. Trendline arrows in direction of increasing tip size.

5.3.2 Dynamic Depth – Combined Plot

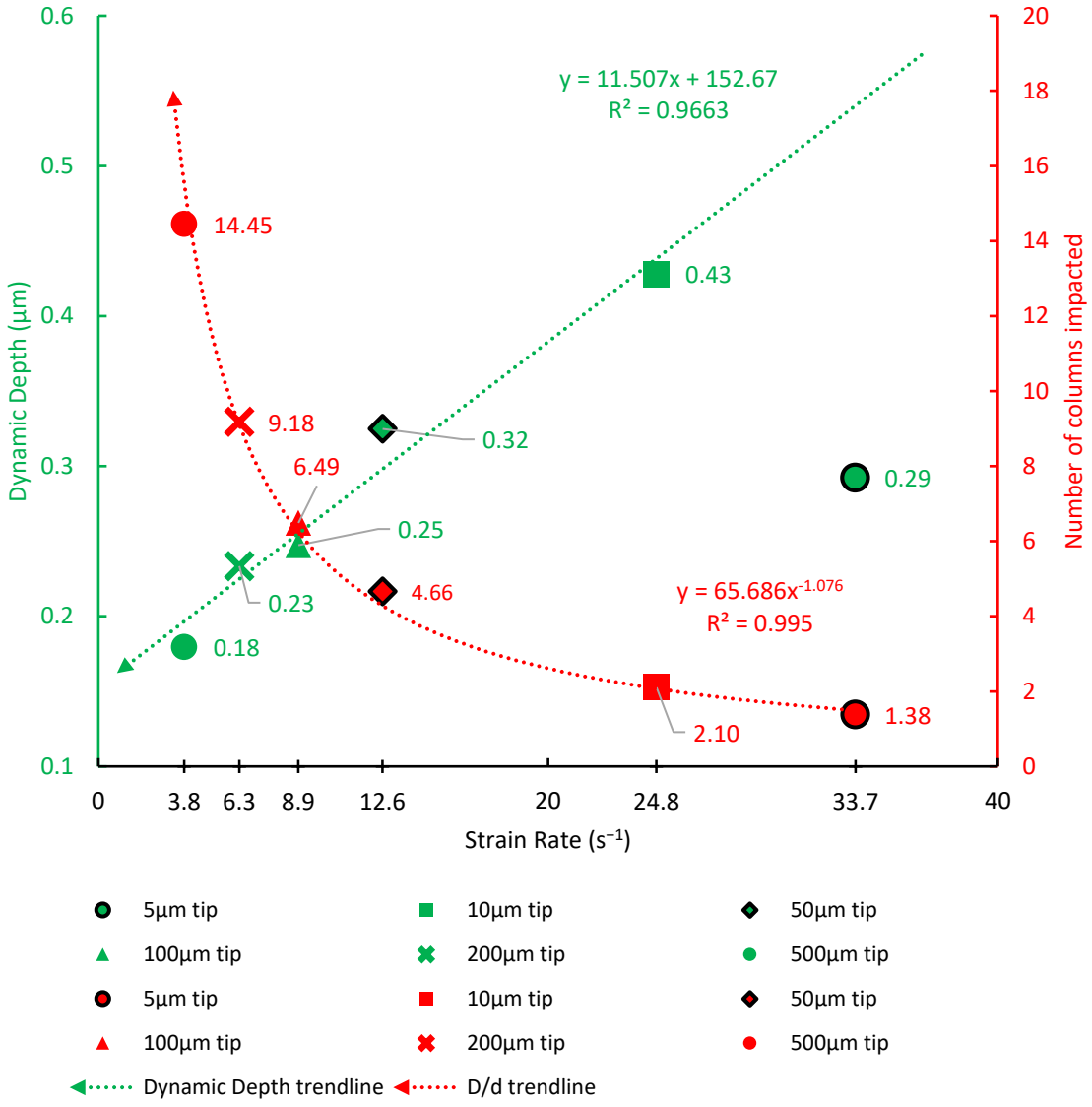

Figure 33: Combined plot showing the relationship between strain rate and *D/d* ratio on dynamic depth. Trendline arrows in direction of increasing tip size.

5.3.3 IMPACT ENERGY – COMBINED PLOT

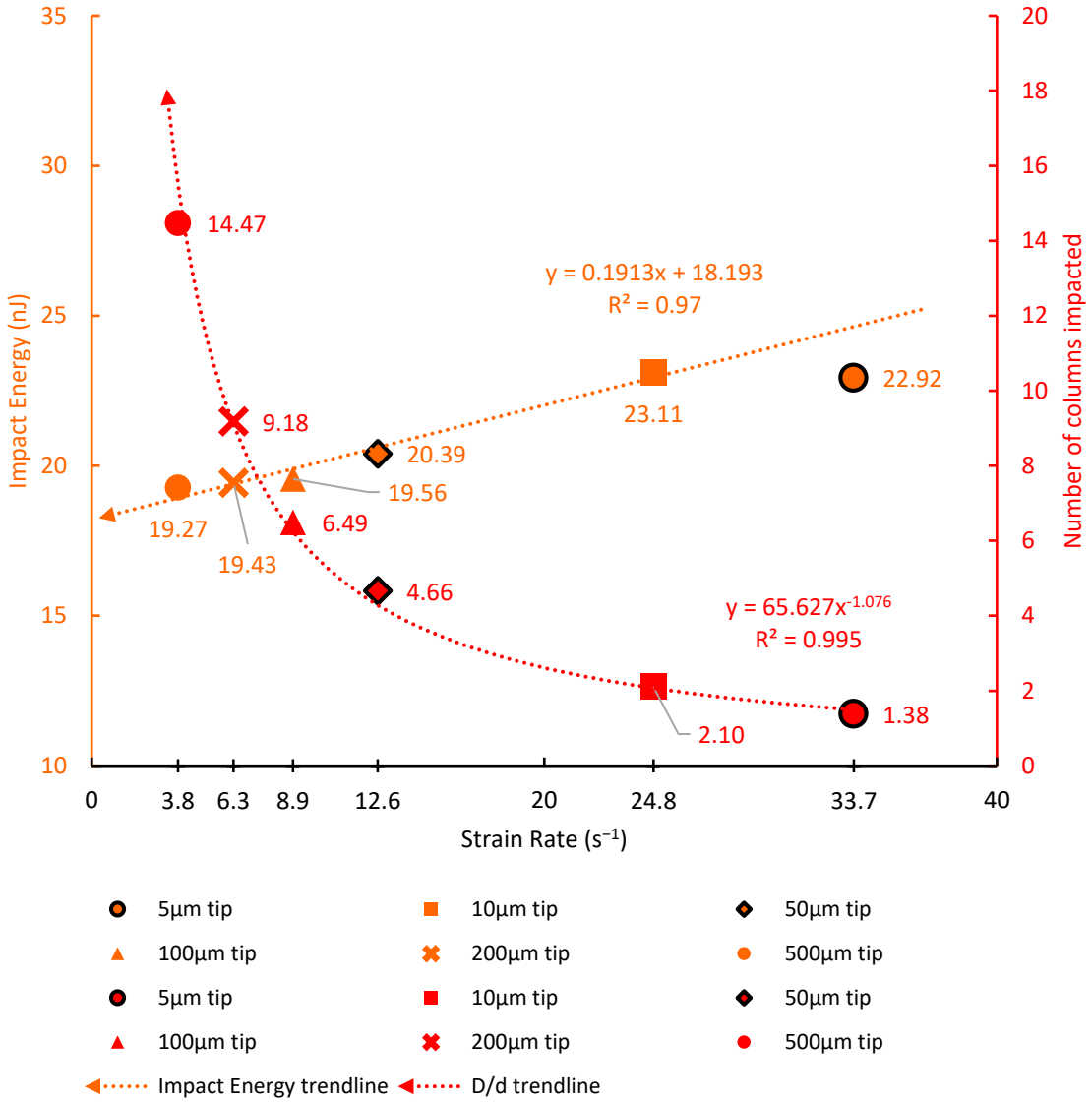

Figure 34: Combined plot showing the relationship between strain rate and *D/d* ratio on Impact energy. Trendline arrows in direction of increasing tip size.

5.3.4 Coefficient of Restitution – Combined Plot

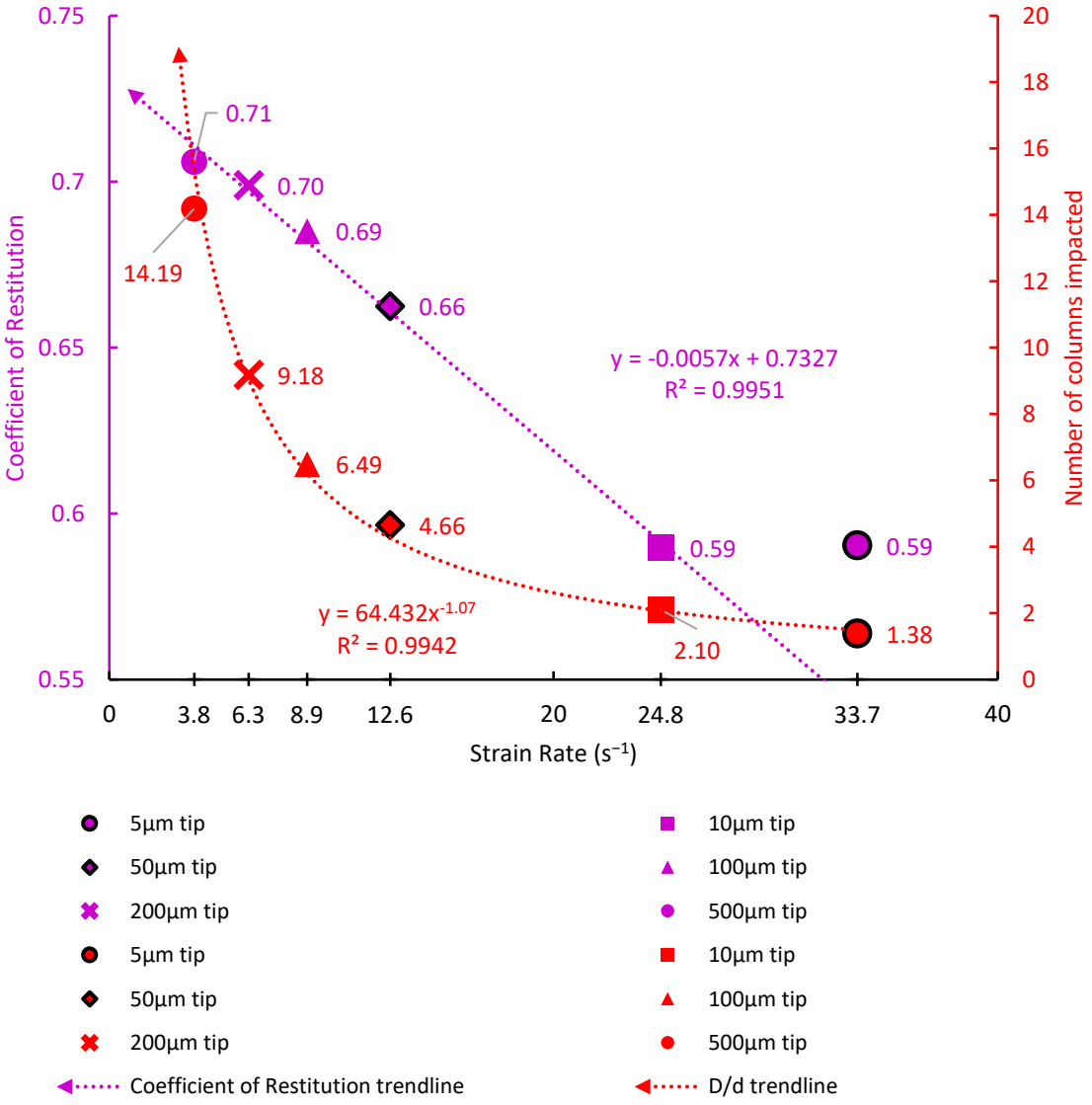

Figure 35: Combined plot showing the relationship between strain rate and *D/d* ratio on *CoR*. Trendline arrows in direction of increasing tip size.

5.4 STRAIN RATE SENSITIVITY

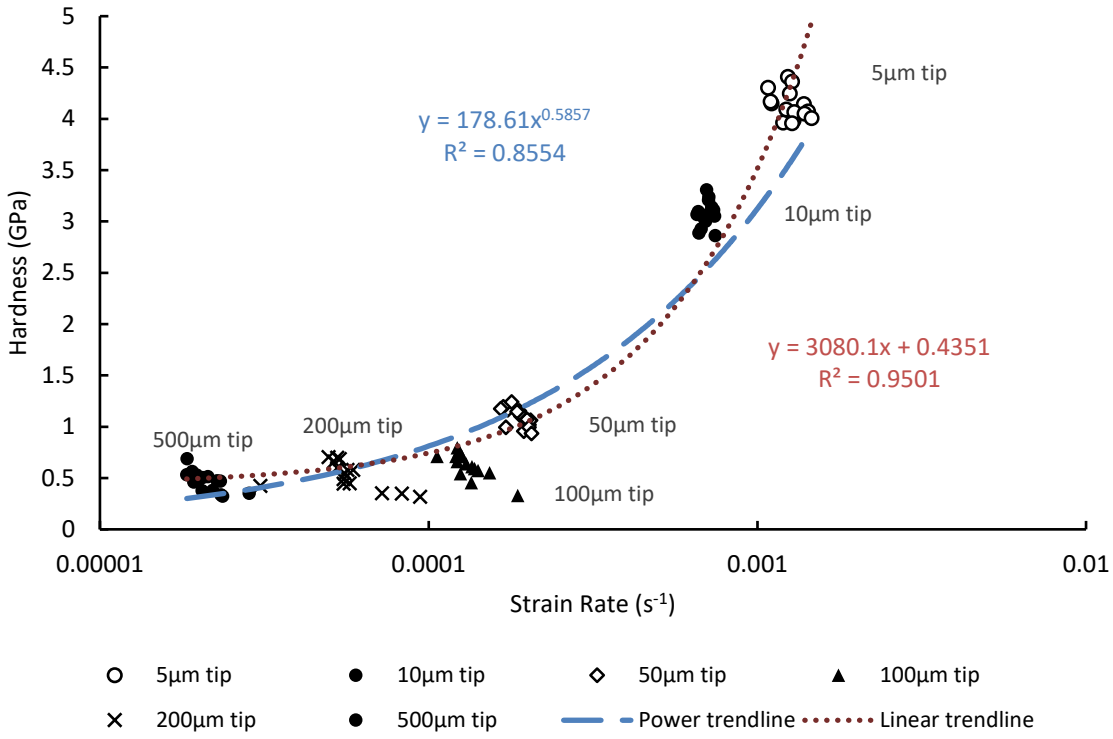

Figure 36: Plot of hardness vs strain rate from nanoindentation data.

From the nanoindentation data, hardness values and strain rates were extracted and plotted in Figure 37. The strain rate values associated with each tip for this study is shown in Table 8. A linear and power line of best fit was fitted through the data. The R^2 values for each fit (shown on the plot) differed by 11%, with the linear equation providing a better fit.

Table 8: Average strain rate values for each tip size from nanoindentation data.

Tip size (µm)	Average strain rate (s^{-1})*
5	1.2670775E-03
10	6.9863125E-04
50	1.8811755E-04
100	1.3274787E-04
200	5.8600602E-05
500	2.1362645E-05

*Strain rate value used is the numerical average of strain rates recorded from the time the nanoindentation started till it reached the maximum depth.

Figure 37 shows the hardness measured at the highest strain rate is significantly higher than the hardness value measured at the lowest strain rate. The curve indicates that hardness decreases with decreasing strain rate till it reaches a plateau.

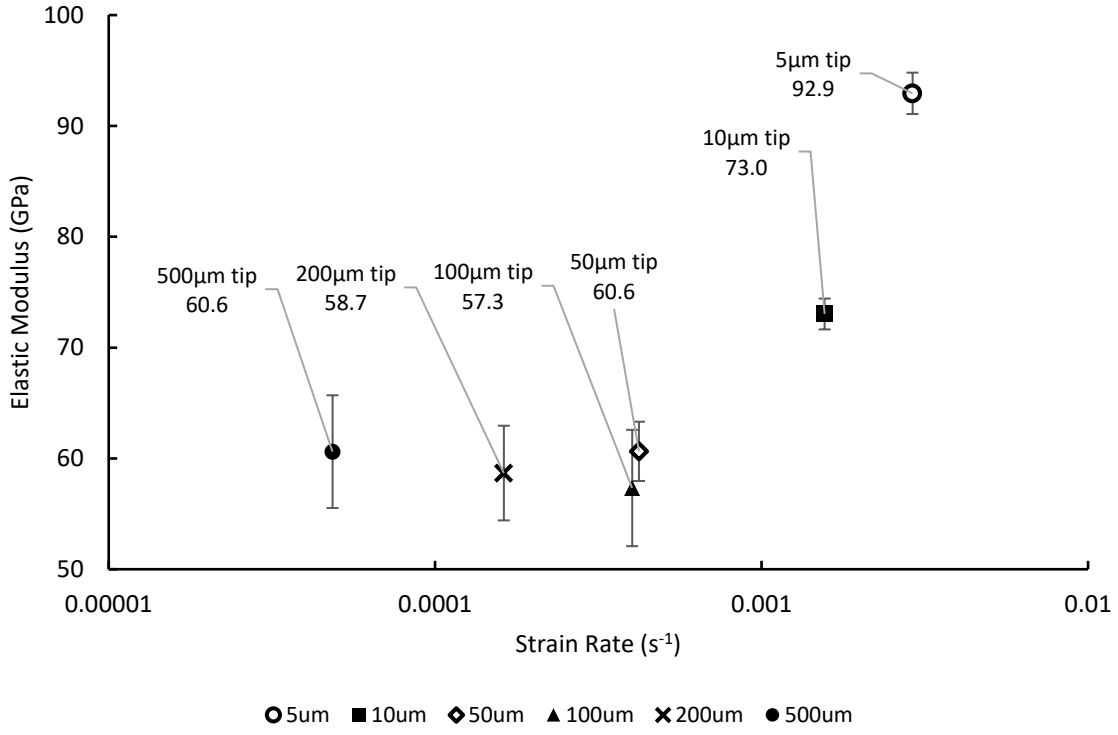

Figure 37: Plot of elastic modulus vs strain rate. Tip size and elastic modulus values rounded up to 1 decimal place are shown in data callouts.

Similarly, the elastic modulus data was plotted against the strain rate in Figure 38. Elastic modulus values of the high strain rate values (caused by small 5µm and 10 µm tips) are significantly higher compared to the low strain rate values below $0.001s^{-1}$. Within these recorded strain rates, the elastic modulus of enamel ranges from 60.6 - 92.9 GPa.

Chapter 6 DISCUSSION

6.1 STRAIN RATE SENSITIVITY

The range of strain rates provided by the 6 tip sizes was extremely small at 0.00001 s^{-1} – 0.001 s^{-1}. Work by Zhang et al [50] and He and Swain [21] used strain rate ranges in the order of 0.01 s^{-1} – 0.1 s^{-1}.

Using Eq. 17, the data from this set of nanoindentations show the *m* value is 0.5857. However, this value may not accurately represent enamel as the strain rate range used is extremely small. Only creep rate sensitivity values were found [21, 69] in literature and were a magnitude lower than the *m* value obtained in this study.

Nevertheless, the change in response of hardness and elastic modulus of the enamel to strain rate is still a measure of strain rate sensitivity. The elastic modulus was at an average of 59.3 GPa between strain rates of 0.00001 s^{-1} – 0.001 s^{-1} and then increased by 21% and 44% when strain rates of 0.0007 s^{-1} and 0.0013 s^{-1} were used. The drastic change in elastic modulus and hardness values with increasing strain rate larger indicates that elastic modulus for enamel is strain rate dependent.

Literature [21, 50] suggests the change in these values with strain rate is due to the creep behaviour of the organic matrix. After initial trials with the liquid cell apparatus mentioned in Chapter 4.3 where the disk was submerged in distilled water, the enamel disk was left to dry in air in room temperature. It is likely some traces of water and active protein remained in between the narrow prisms of the enamel when the next set of nanoimpacts was conducted. This is backed up by Habelitz [12] who suggests minimal amount of protein still affects the mechanical properties at nanofibril-level.

Low strain rate (0.0001s-1) mechanical testing of trabecular bone by Linde et al [70] showed similar trends in the change of elastic modulus and hardness observed in this experiment. Enamel and trabecular bone possess different structures that result in vastly different values of elastic modulus and hardness. but the trends are similar as they are both calcified tissues.

6.2 STRAIN RATES

The strain rate is a measure of how much damage is being done to the enamel, as a high strain rate indicates the tip is effectively penetrating deeper into the tissue according to Equation 3 and Equation 4. Strain rates in this study were varied by using spherical tips of different radiuses. A smaller tip produces a larger strain rate compared to a larger tip.

The dynamic hardness values increase dramatically for higher strain rates compared to lower strain rates, as the results for the 5µm and 10µm tip are significantly higher than the larger tips. This visualized by the gradients of the linear regression lines in Figure 23.

Looking at Figures 32-35, the relationship between values of the dependent variables and strain rates have strong linear relationships ($R^2 > 0.95$) except for the 5µm tip which does not fit the line. Furthermore, Figures 27,30,33 all show a clear inflexion point between the 5µm tip and 10µm.

The inflexion points and behaviour of the small tips can be explained using the *D/d* ratio.

6.3 D/D RATIO

The *D/d* ratio is a measure of how the structure of the material is affected. In this experiment, the *D/d* ratio is interchangeable with number of columns impacted by the indenter, as explained in Chapter 4.4.2. The test matrix outlined in Table 3 was chosen to allow for a *D/d* range of 0-20 as Wellman and Nicholls [52] had recorded. The coloured zones mark the transition between different damage mechanisms according to the thresholds explained in Chapter 3.7.

Inflexion points found between the 5µm tip and 10µm tip from Chapter 5.1 with the strain rate plots also appear in the *D/d* plots. The columnar structure of the enamel rods plays a role in its damage mechanisms and causes these inflexion points.

The number of enamel rods a tip interacts with (this number being the *D/d* ratio) increases as the size of the tip increases. This is seen in Figures 27,29,30,31 where the smaller 5µm and 10µm tips have a *D/d* ratio of 1-2, while the large 500 µm tip used is mostly scattered in the *D/d* ratio above 12 and the remaining tips stay between a *D/d* ratio of 2-12. A visual of the tip-column interaction is shown in Figure 38.

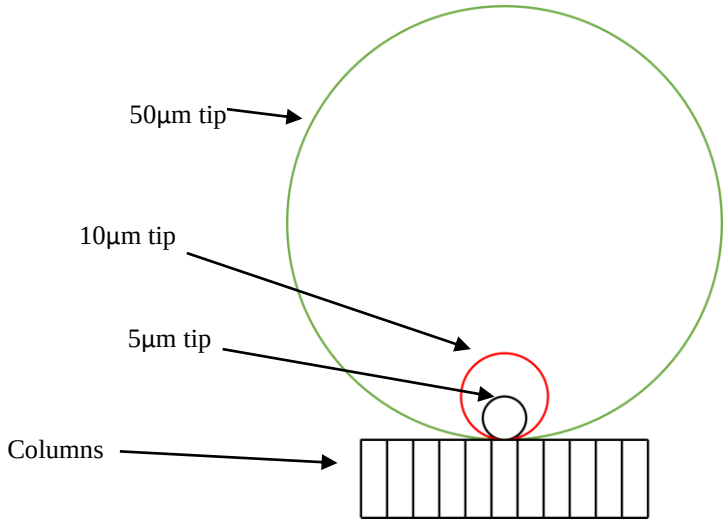

Figure 38: Illustration (not to scale) of increasing tip sizes (tip size corresponds to radius of sphere) and the number of columns they interact with.

6.3.1 SINGLE COLUMN RESPONSE VS MULTI-COLUMN RESPONSE

This single column versus multi-column (>2) response of different tip sizes is the structural effect of the enamel that influences the measured values at different *D/d* ratios.

For example, when measuring dynamic hardness, the 5µm tip is only measuring the hardness of a single column, meanwhile, the large 500µm tip interacts with multiple columns causing greater system compliance and results in a lower measured dynamic harness.

In the plots against *D/d* ratio for Impact energy (Figure 29) and dynamic depth (Figure 30), the 10µm tip which hits around 2+ columns has an average value of 23.1nJ and 0.43µm respectively which then decreases linearly (see Figure 33 and Figure 34) to the average value of 19.3nJ and 0.18µm when the 500µm tip hits 14 columns. The plot of *CoR* versus *D/d* ratio is unique as the *CoR* value increases, showing a greater elastic response as the number of columns impacted increases from 2 to 9 (10µm tip – 200µm tip) then appears to plateau, with the an impact involving 14 columns (500µm tip) recording the same *CoR* value as the 200µm tip to 2 d.p (see Figure 35)

6.3.2 KEYHOLE STRUCTURE OF ENAMEL PRISMS

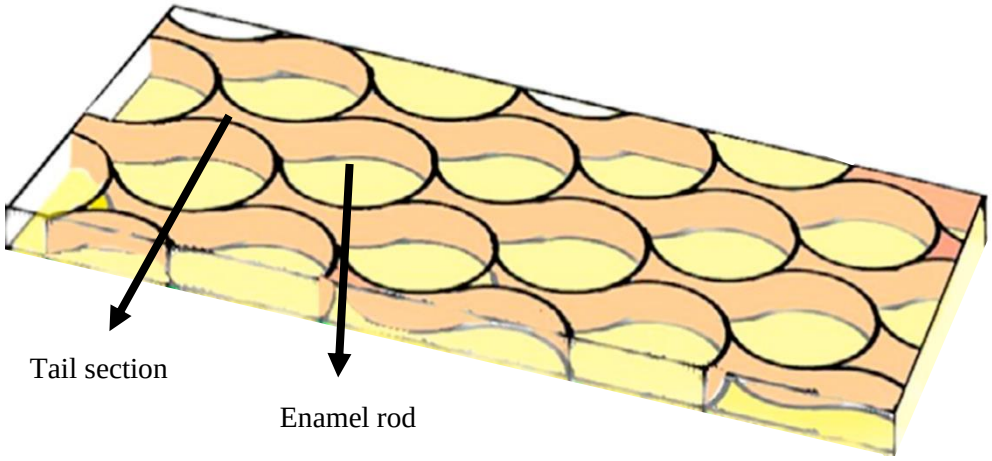

Figure 39: Illustration of the keyhole shape of enamel prisms. Adapted from Cheng et al [71].

The inflexion point observed between the 5µm tip and 10µm tip for the dependent variables in Figures 22,24,25,26 can be attributed to the keyhole structure of the enamel rods.

The 5µm tip interacts with a single column (< 2 at most) as shown from the *D/d* plots in Chapter 5.2. As this tip is small, there is a potential that it is hitting the interfaces between the enamel rods: the tail section, which has a lower elastic modulus, Hardness and imperfect alignment of HAP crystals compared to the enamel rods [14, 15]. The 5µm tip interrogates the surface differently because it may hit either a rod or tail section and record a different measured value compared to the larger 10µm tip that hits a combination of rod and tail section.

As enamel is a biological tissue, naturally, distributions in the data would be expected. In Chapter 4.6.1, the 5µm tip shows a larger distribution of dynamic hardness values compared to the other tips. This can be seen in Figure 40 where the distribution of measured hardness of the small 5µm tip is significantly bigger than that of the larger tips. The noise in the 5µm tip data could be due to the keyhole structure of the enamel prisms.

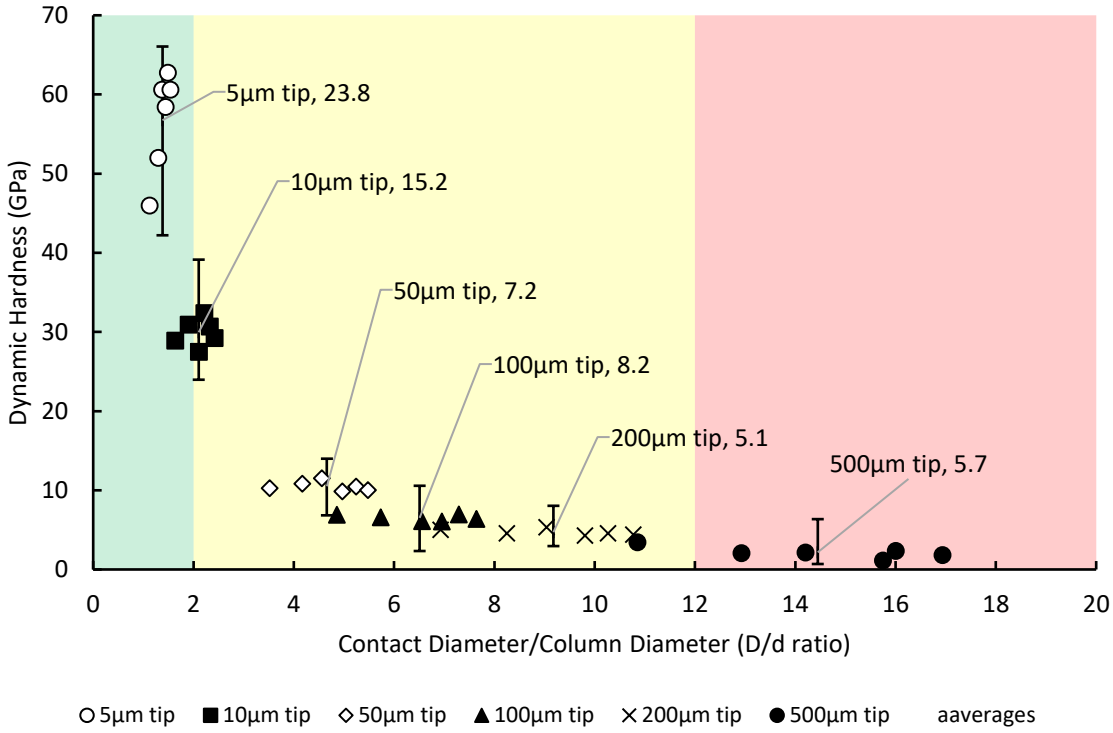

Figure 40: Plot of dynamic hardness vs *D/d* ratio with data callouts for tip size and the difference between the highest and lowest dynamic hardness recorded by that tip..

Large tips have a multi-column response (high *D/d* ratio) and interact with a combination of tail sections and enamel rods which even outs the distribution measured hardness as the number of columns the indenter acts on increases.

This can explain the variability of the *CoR* values between *D/d* ratio of 2-12 as the tips gradually start hitting less of the interfaces and more of the enamel rods, the *CoR* value eventually levels off after 12 columns have been hit.

6.4 DAMAGE MECHANISMS OBSERVED IN ENAMEL AND COMPARISON WITH EB-PVD.

The *D/d* ratio threshold values of 0-2, 2-12, and 12-20 proposed by Wellman and Nicholls in his work with determining different damage mechanisms for EB-PVD's have translated well in showing the transitions between different damage mechanisms in enamel. The coloured zones from *D/d* ratio plots in Chapter 5.2 show the categorization of the 5μm and 10μm tip into the 0-2 *D/d* range, 50,100,200μm tip into the 2-12 *D/d* range and 500μm tip into the 12-20 *D/d* range.

The 3 damage mechanisms in order of increasing *D/d* ratio are Erosion, Compaction, and FOD proposed by Wellman and Nicholls (explained in Chapter 3.7) seem to be reversed in enamel; with FOD, Compaction and Erosion taking place with increasing *D/d* ratio.

For enamel, the *D/d* ratio range of 0-2 shows the highest penetration depths, impact energies, and low elastic response. Compared to the *D/d* ratio range of 12-20, the impact is shallower with the lowest impact energies and much more elastic in terms of the response. This indicates that the 0-2 *D/d* range is when the most damage and material loss is being done to the enamel structure compared to the 2-12 *D/d* range where the structural integrity might not be affected too much. From the view of the air abrasion device, a smaller particle would damage the enamel surface more compared to a larger particle travelling at the same velocity. For EB-PVDs, these types of damage occur at the opposite ends of the *D/d* ratio scale.

This disconnect between the different results could be due to the different mass of particles used for impacting the surface. If a big particle and small particle are matched with the same velocity, the big particle which has a bigger mass and higher energy on impact would deal more damage and interact with more columns than the small particle. Wellman and Nicholls had used 100μm alumina particles at a much higher impact velocity ($>140ms^{-1}$).

Furthermore, Wellman and Nicholls had the opportunity to cut the samples and view the actual damage done to the enamel, but this unfortunately couldn't be carried out in this experiment (see Chapter 10). It is possible that with enamel, the impacts at 12-20 *D/d* range could be carrying out a mix of compaction and surface erosion, effectively leaving a dent on the surface while the impacts at 0-2 *D/d* range are carrying out FOD which penetrates deep into the enamel and fractures the HAP crystals that make up the enamel rods. A small tip size that could cause cracking of the enamel may also introduce other wear mechanisms such as micro-chipping if the HAP crystals are fractured [13, 72].

From a strain rate perspective, the use of different sized tips has managed to test enamel's response to different strain rates, but different tip sizes have not been matched to each other's strain rates. An example is shown in Figure 41 where the 500μm tip's strain rate could be matched to the 5μm tip's

strain rate by firing the 500µm tip at a higher velocity. Not matching the strain rates of tips is another potential difference between the work done in this experiment and Wellman and Nicholls' paper. The 500µm tip firing at a higher velocity to match the strain rates produced by the 5µm tip would result in much more damage to the enamel tissue due to the bigger size and impact energies and possibly agreeing with their findings. In Wellman and Nicholls' work, only one tip size was used, effectively testing the enamel's response to the impacts at the same strain rate.

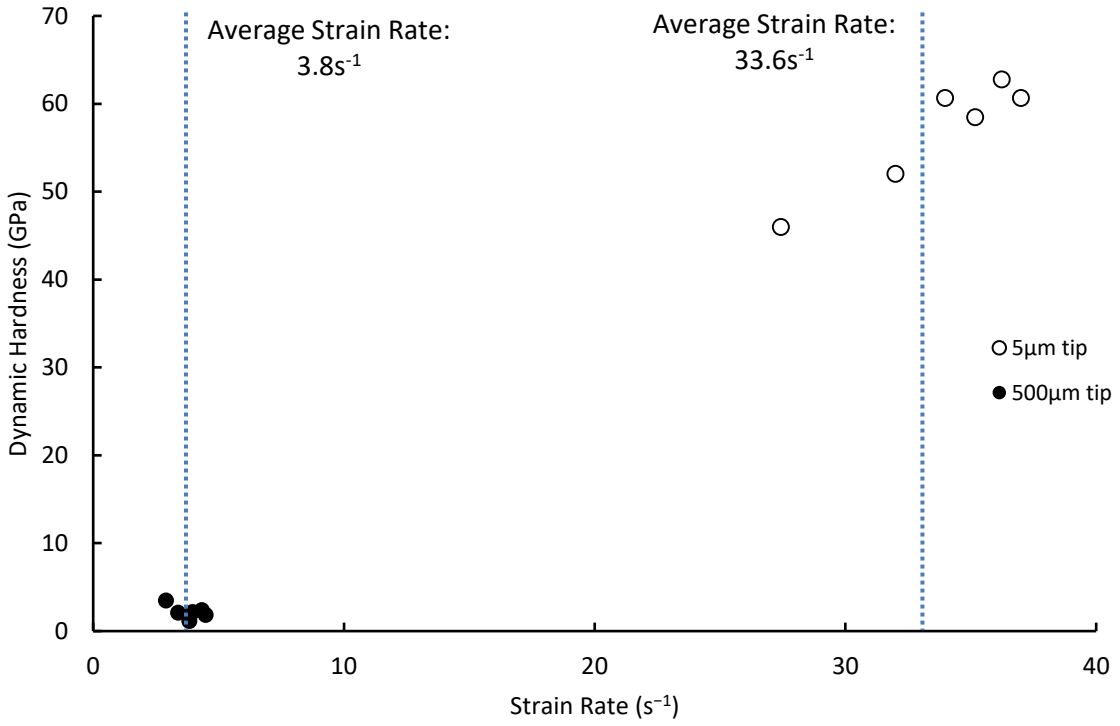

Figure 41: Plot of dynamic hardness vs strain rate that shows the difference in average strain rate values of 5µm tip and 500µm tip.

6.5 DEHYDRATION OF ENAMEL

The literature from Chapter 3.6 shows that the mechanical properties of enamel change significantly when tested under hydrated/dehydrated conditions. Dehydration of calcified tissues such as cortical bone results in an increase in measured hardness and elastic modulus values [73, 74]. The elastic modulus and hardness values recorded from the nanoindentations of enamel in this study are shown in Table 9.

Table 9: Values for elastic modulus and hardness for enamel under hydrated/dehydrated conditions.

Conditions	Elastic modulus, E (GPa)	Hardness, H (GPa)	Author	Maximum depth/load used
Hydrated	87.5 ± 2.1	3.8 ± 0.3	Habelitz [12]	1500 μN; 300nm
	83.4 ± 7.1 (prism) 39.5 ± 4. (sheath	4.3 ± 0.8 (prism) 1.1 ± 0.3 (sheath)	Ge [14]	1000μN (prism) 300μN (sheath)
Dehydrated	60.6 - 92.9	0.46 - 4.13		

The maximum elastic modulus and hardness values recorded are 6.2% and 8.7% higher respectively compared to the hydrated samples, thus following the trend exhibited by bone.

Dehydration of the enamel may have affected the *CoR* values as it alters the enamel's energy absorption capabilities. The presence of the proteins could have enabled the enamel to absorb more energy from the impact through a sacrificial bond [28] and the organic matter's capability to spread the damage over a large volume [75]; as well as letting it recover after unloading to prevent further deformation.

In this experiment, the enamel samples were tested under hydrated conditions but did not output useful data due to errors with the apparatus.

Chapter 7 LIMITATIONS

The primary limitation of this study is the failure of the liquid cell apparatus (see Figure 13) to output accurate results as briefly mentioned in Chapter 4.3. Fluid interactions with the tip manifested as an unusual 'hump' in the plotted data by the MicroMaterials control software, when it should have been a straight line. This faulty data then affected the subsequent results and was not a reliable way of collecting correct information from the nanoimpacts.

Stiffening the arm of the pendulum system connected to the indenter may have resolved the hump but was not done as it was outside the scope of this experiment.

Despite troubleshooting efforts and applying different test matrixes, the faulty data kept reappearing. In the interest of time, the decision was then made to carry out the entire test matrix again under dry conditions without a liquid cell apparatus.

Some data collected at the initial phase of this study with the liquid cell apparatus have been included in Appendix B.

Chapter 8 DISRUPTIONS DUE TO COVID-19

Due to COVID-19, serial polishing of the enamel disk to examine the subsurface damage could not be carried out due to the university's shutdown.

The impacted sample was to be embedded in cold cure resin, followed by serially polishing of the working surface to visualize the subsurface damage to the enamel microstructure using an SEM. The purpose is to check if the damage observed in the enamel matched the damage types by Wellman [52] in relation to the erosion theories.

Chapter 9 FUTURE WORK

Future repetitions of this experiment should use hydrated enamel sample as opposed to dry samples to observe differences in the erosion mechanisms. Hydration of the sample causes the proteins present in the enamel tissue to play a significant role [21] and may affect the enamel's mechanical response.

Additionally, matching the strain rates of the different tip sizes together to enable better comparison with Wellman and Nicholls' work.

Visual inspection of the impact damage to the enamel surface under SEM should also be carried out to verify any link between the types of damage on the enamel microstructure from different impact scenarios to Wellman and Nicholls' erosion theories [52].

Chapter 10 CONCLUSION

In conclusion, this experiment has studied the impact response of bovine enamel to different particle geometries and strain rates using nanoimpacts and nanoindentation to simulate a commercial air abrasion system. All dependent variables: dynamic hardness, dynamic depth, impact energy, and coefficient of restitution had shown strong linear relationships with increasing strain rate up until an inflexion point was reached with the 5μm radius spherical indenter.

This suggested the underlying structure of enamel affected the mechanical response too. The *D/d* ratio, a concept introduced by Wellman and Nicholls [52] in their work with EB-PVD TBCs were used to study the erosion behaviour of enamel due to similarities in their columnar microstructure. The mechanical response of the enamel tissue was found to vary with both the strain rates and *D/d* ratios. The inflexion points observed with the strain rates occurred at a *D/d* ratio of less than 2. The *D/d* ratio in this study also directly related to the number of columns impacted, suggesting that different particle geometries affect the erosion mechanism of enamel. Small particles close to the size of the enamel prims elicited a single column response while larger particle elicited a multi-column response. The keyhole shape of enamel prisms is the reason behind the inflexion points as the small 5μm indenter likely interacted with the interfaces between enamel rods that have different HAP crystal orientations compared to the enamel rods, causing the inflexion point.

The *D/d* ratio thresholds studied by Wellman and Nicholls [52] that identify different erosion regimes in TBCs were found to fit for enamel as well. However, impact data indicated the type of damage that occurs between the prescribed *D/d* thresholds for enamel appears to the opposite of TBCs. From the view of the air abrasion perspective, using the data observed it is found that a larger particle would cause lesser damage than a small particle traveling at the same velocity.

From nanoindentation of the enamel, hardness and elastic modulus of enamel were found to be strain rate dependent, which is supported in literature for enamel tested under hydrated conditions. As the enamel tested in this experiment was not tested under hydrated conditions, air-drying the sample may have left trace amounts of water and proteins in the enamel structure.

This experiment has shown that nanoimpact and nanoindentation testing are useful tools to understand the parameters of the air abrasion process and how they affect the erosion mechanisms of enamel better. Future undertakings need to ensure the enamel is tested under fully hydrated conditions, the mass of particles accounted for, and strain rates of different sized spherical indenters are matched to each other. The actual subsurface damage to the enamel must be checked under SEM for comparison with Wellman and Nicholls' [52] observations.

LIST OF REFERENCES

[1] R. H. Selwitz, A. I. Ismail, and N. B. Pitts, "Dental caries," (in eng), *Lancet*, vol. 369, no. 9555, pp. 51-9, Jan 6 2007, doi: https://doi.org/10.1016/s0140-6736(07)60031-2.

[2] *NHS Dental Statistics for England 2019-20, Biannual Report*. [Online] Available: https://digital.nhs.uk/data-and-information/publications/statistical/nhs-dental-statistics/2019-20-biannual-report

[3] H. M. Wong, C. M. Mak, and Y. F. Xu, "A four-part setting on examining the anxiety-provoking capacity of the sound of dental equipment," *Noise and Health*, vol. 13, no. 55, p. 385, 2011.

[4] *AquaCare - Dentistry's New Norm*. (2019). United Kingdom: Medivance Instruments Ltd. Accessed: 30 April 2020. [Online]. Available: https://optident.co.uk/app/uploads/2019/01/AquacareDigitalBrochure0918-Mobile.pdf

[5] C. Mercer, J. Williams, D. Clarke, and A. Evans, "On a Ferroelastic Mechanism Governing The Toughness of Metastable Tetragonal-Prime Yttria-Stabilized Zirconia," *Proceedings of The Royal Society A: Mathematical, Physical and Engineering Sciences*, vol. 463, pp. 1393-1408, 05/08 2007, doi: https://doi.org/10.1098/rspa.2007.1829.

[6] R. Darolia, "Thermal barrier coatings technology: critical review, progress update, remaining challenges and prospects," *International Materials Reviews*, vol. 58, no. 6, pp. 315-348, 2013/08/01 2013, doi: https://doi.org/10.1179/1743280413Y.0000000019.

[7] A. Giannakopoulos, A. Kordolemis, and T. Zisis, "Development of Strong Surfaces Using Functionally Graded Composites Inspired by Natural Teeth—A Theoretical Approach," *Journal of Engineering Materials and Technology-transactions of The Asme - J ENG MATER TECHNOL*, vol. 132, 01/01 2010, doi: https://doi.org/10.1115/1.3184037.

[8] L.-H. He and M. Swain, "Enamel-A functionally graded natural coating," *Journal of dentistry*, vol. 37, pp. 596-603, 05/01 2009, doi: https://doi.org/10.1016/j.jdent.2009.03.019.

[9] L. H. He and M. V. Swain, "Enamel - a "metallic-like" deformable biocomposite," (in eng), *J Dent*, vol. 35, no. 5, pp. 431-7, May 2007, doi: https://doi.org/10.1016/j.jdent.2006.12.002.

[10] A. J. Gwinnett, "Structure and composition of enamel," (in eng), *Oper Dent*, vol. Suppl 5, pp. 10-7, 1992.

[11] E. Beniash *et al.*, "The hidden structure of human enamel," *Nature Communications*, vol. 10, no. 1, p. 4383, 2019/09/26 2019, doi: https://doi.org/10.1038/s41467-019-12185-7.

[12] S. Habelitz, S. J. Marshall, G. W. Marshall, Jr., and M. Balooch, "Mechanical properties of human dental enamel on the nanometre scale," (in eng), *Arch Oral Biol*, vol. 46, no. 2, pp. 173-83, Feb 2001, doi: https://doi.org/10.1016/s0003-9969(00)00089-3.

[13] J. Zheng, Y. Li, M. Y. Shi, Y. F. Zhang, L. M. Qian, and Z. R. Zhou, "Microtribological behaviour of human tooth enamel and artificial hydroxyapatite," *Tribology International*, vol. 63, pp. 177-185, 2013/07/01/ 2013, doi: https://doi.org/10.1016/j.triboint.2012.04.019.

[14] J. Ge, F. Z. Cui, X. M. Wang, and H. L. Feng, "Property variations in the prism and the organic sheath within enamel by nanoindentation," (in eng), *Biomaterials*, vol. 26, no. 16, pp. 3333-9, Jun 2005, doi: https://doi.org/10.1016/j.biomaterials.2004.07.059.

[15] H. Warshawsky, "Organization of crystals in enamel," *The Anatomical Record*, vol. 224, no. 2, pp. 242-262, 1989/06/01 1989, doi: https://doi.org/10.1002/ar.1092240214.

[16] M. C. Maas and E. R. Dumont, "Built to last: The structure, function, and evolution of primate dental enamel," *Evolutionary Anthropology: Issues, News, and Reviews*, vol. 8, no. 4, pp. 133-152, 1999/01/01 1999, doi: https://doi.org/10.1002/(SICI)1520-6505(1999)8:4<133::AID-EVAN4>3.0.CO;2-F.

[17] S. Bechtle *et al.*, "Hierarchical flexural strength of enamel: Transition from brittle to damage-tolerant behaviour," *Journal of the Royal Society, Interface / the Royal Society*, vol. 9, pp. 1265-74, 10/26 2011, doi: https://doi.org/10.1098/rsif.2011.0498.

[18] J. Zhou and L. Hsiung, "Depth-dependent mechanical properties of enamel by nanoidentation," *Journal of biomedical materials research. Part A*, vol. 81, pp. 66-74, 04/01 2007, doi: https://doi.org/10.1002/jbm.a.31012.

[19] J. L. Cuy, A. B. Mann, K. J. Livi, M. F. Teaford, and T. P. Weihs, "Nanoindentation mapping of the mechanical properties of human molar tooth enamel," *Archives of Oral Biology*, vol. 47, no. 4, pp. 281-291, 2002/04/01/ 2002, doi: https://doi.org/10.1016/S0003-9969(02)00006-7.

[20] L. He and M. Swain, "Energy absorption characterization of human enamel using nanoindentation," *Journal of biomedical materials research. Part A*, vol. 81, pp. 484-92, 05/01 2007, doi: https://doi.org/10.1002/jbm.a.31051.

[21] L.-H. He and M. Swain, "Nanoindentation creep behavior of human enamel," *Journal of biomedical materials research. Part A*, vol. 91, pp. 352-9, 11/01 2009, doi: https://doi.org/10.1002/jbm.a.32223.

[22] J. Zheng, Y. Zeng, J. Wen, L. Zheng, and Z. Zhou, "Impact wear behavior of human tooth enamel under simulated chewing conditions," *Journal of the Mechanical Behavior of*

Biomedical Materials, vol. 62, pp. 119-127, 2016/09/01/ 2016, doi: https://doi.org/10.1016/j.jmbbm.2016.04.039.

[23] J. Zheng, Y. Huang, L. Qian, and Z. Zhou, "Nanomechanical properties and microtribological behaviours of human tooth enamel," *Proceedings of The Institution of Mechanical Engineers Part J-journal of Engineering Tribology - PROC INST MECH ENG J-J ENG TR*, vol. 224, pp. 577-587, 06/01 2010, doi: https://doi.org/10.1243/13506501JET693.

[24] M. Yahyazadehfar and D. Arola, "The role of organic proteins on the crack growth resistance of human enamel," *Acta Biomaterialia*, vol. 19, pp. 33-45, 2015/06/01/ 2015, doi: https://doi.org/10.1016/j.actbio.2015.03.011.

[25] P. G. Fox, "The toughness of tooth enamel, a natural fibrous composite," *Journal of Materials Science*, vol. 15, no. 12, pp. 3113-3121, 1980/12/01 1980, doi: https://doi.org/10.1007/BF00550384.

[26] E. C. Moreno and R. T. Zahradnik, "The pore structure of human dental enamel," (in eng), *Arch Oral Biol*, vol. 18, no. 8, pp. 1063-8, Aug 1973, doi: https://doi.org/10.1016/0003-9969(73)90187-8.

[27] L. H. He and M. V. Swain, "Influence of environment on the mechanical behaviour of mature human enamel," (in eng), *Biomaterials*, vol. 28, no. 30, pp. 4512-20, Oct 2007, doi: https://doi.org/10.1016/j.biomaterials.2007.06.020.

[28] M. Rief, M. Gautel, F. Oesterhelt, J. M. Fernandez, and H. E. Gaub, "Reversible unfolding of individual titin immunoglobulin domains by AFM," (in eng), *Science*, vol. 276, no. 5315, pp. 1109-12, May 16 1997, doi: https://doi.org/10.1126/science.276.5315.1109.

[29] J. B. Thompson, J. H. Kindt, B. Drake, H. G. Hansma, D. E. Morse, and P. K. Hansma, "Bone indentation recovery time correlates with bond reforming time," (in eng), *Nature*, vol. 414, no. 6865, pp. 773-6, Dec 13 2001, doi: https://doi.org/10.1038/414773a.

[30] G. E. Fantner *et al.*, "Sacrificial bonds and hidden length dissipate energy as mineralized fibrils separate during bone fracture," (in eng), *Nat Mater*, vol. 4, no. 8, pp. 612-6, Aug 2005, doi: https://doi.org/10.1038/nmat1428.

[31] G. A. Macho, Y. Jiang, and I. R. Spears, "Enamel microstructure--a truly three-dimensional structure," (in eng), *J Hum Evol*, vol. 45, no. 1, pp. 81-90, Jul 2003, doi: https://doi.org/10.1016/s0047-2484(03)00083-6.

[32] J. L. Katz and K. Ukraincik, "On the anisotropic elastic properties of hydroxyapatite," *Journal of Biomechanics*, vol. 4, no. 3, pp. 221-227, 1971/05/01/ 1971, doi: https://doi.org/10.1016/0021-9290(71)90007-8.

[33] I. Spears, "A Three-dimensional Finite Element Model of Prismatic Enamel: A Re-appraisal of the Data on the Young's Modulus of Enamel," *Journal of dental research*, vol. 76, pp. 1690-7, 11/01 1997, doi: https://doi.org/10.1177/00220345970760101101.

[34] H. Gao, "Mechanical properties of nanostructure of biological materials," *Journal of the Mechanics and Physics of Solids*, vol. 52, pp. 1963-1990, 09/01 2004, doi: https://doi.org/10.1016/j.jmps.2004.03.006.

[35] M. Staines, W. H. Robinson, and J. A. A. Hood, "Spherical indentation of tooth enamel," *Journal of Materials Science*, vol. 16, no. 9, pp. 2551-2556, 1981/09/01 1981, doi: https://doi.org/10.1007/BF01113595.

[36] H. Jiang, X.-Y. Liu, C. T. Lim, and C.-Y. Hsu, "Ordering of self-assembled nanobiominerals in correlation to mechanical properties of hard tissues," *Applied Physics Letters*, vol. 86, pp. 163901-163901, 04/13 2005, doi: https://doi.org/10.1063/1.1906295.

[37] H. Fong, M. Sarikaya, S. N. White, and M. L. Snead, "Nano-mechanical properties profiles across dentin–enamel junction of human incisor teeth," *Materials Science and Engineering: C*, vol. 7, no. 2, pp. 119-128, 1999/12/01/ 1999, doi: https://doi.org/10.1016/S0928-4931(99)00133-2.

[38] H. H. Xu *et al.*, "Indentation damage and mechanical properties of human enamel and dentin," (in eng), *J Dent Res*, vol. 77, no. 3, pp. 472-80, Mar 1998, doi: https://doi.org/10.1177/00220345980770030601.

[39] S. Park, D. H. Wang, D. Zhang, E. Romberg, and D. Arola, "Mechanical properties of human enamel as a function of age and location in the tooth," *Journal of Materials Science: Materials in Medicine*, vol. 19, no. 6, pp. 2317-2324, 2008, doi: https://doi.org/10.1007/s10856-007-3340-y.

[40] H. M. Elfallah, L. E. Bertassoni, N. Charadram, C. Rathsam, and M. V. Swain, "Effect of tooth bleaching agents on protein content and mechanical properties of dental enamel," *Acta Biomaterialia*, vol. 20, pp. 120-128, 2015/07/01/ 2015, doi: https://doi.org/10.1016/j.actbio.2015.03.035.

[41] G. Willems, J. P. Celis, P. Lambrechts, M. Braem, and G. Vanherle, "Hardness and Young's modulus determined by nanoindentation technique of filler particles of dental restorative

materials compared with human enamel," (in eng), *J Biomed Mater Res*, vol. 27, no. 6, pp. 747-55, Jun 1993, doi: https://doi.org/10.1002/jbm.820270607.

[42] E. Mahoney, A. Holt, M. Swain, and N. Kilpatrick, "The hardness and modulus of elasticity of primary molar teeth: an ultra-micro-indentation study," (in eng), *J Dent*, vol. 28, no. 8, pp. 589-94, Nov 2000, doi: https://doi.org/10.1016/s0300-5712(00)00043-9.

[43] R. P. Shellis and G. H. Dibdin, "Enamel microporosity and its functional implications," in *Development, Function and Evolution of Teeth*, M. F. Teaford, M. W. J. Ferguson, and M. Meredith Smith Eds. Cambridge: Cambridge University Press, 2000, pp. 242-251.

[44] E. Bonte, N. Deschamps, M. Goldberg, and V. Vernois, "Quantification of Free Water in Human Dental Enamel," *Journal of dental research*, vol. 67, pp. 880-2, 06/01 1988, doi: https://doi.org/10.1177/00220345880670051701.

[45] A. Banerjee, I. D. Thompson, and T. F. Watson, "Minimally invasive caries removal using bio-active glass air-abrasion," *Journal of Dentistry*, vol. 39, no. 1, pp. 2-7, 2011/01/01/ 2011, doi: https://doi.org/10.1016/j.jdent.2010.09.004.

[46] L. H. He and M. V. Swain, "Nanoindentation derived stress-strain properties of dental materials," (in eng), *Dent Mater*, vol. 23, no. 7, pp. 814-21, Jul 2007, doi: https://doi.org/10.1016/j.dental.2006.06.017.

[47] M. Baldassarri, H. C. Margolis, and E. Beniash, "Compositional determinants of mechanical properties of enamel," (in eng), *Journal of dental research*, vol. 87, no. 7, pp. 645-649, 2008, doi: https://doi.org/10.1177/154405910808700711.

[48] V. Maier-Kiener and K. Durst, "Advanced Nanoindentation Testing for Studying Strain-Rate Sensitivity and Activation Volume," *JOM*, vol. 69, no. 11, pp. 2246-2255, 2017/11/01 2017, doi: https://doi.org/10.1007/s11837-017-2536-y.

[49] A. G. Atkins and D. Tabor, "Plastic indentation in metals with cones," *Journal of the Mechanics and Physics of Solids*, vol. 13, no. 3, pp. 149-164, 1965/06/01/ 1965, doi: https://doi.org/10.1016/0022-5096(65)90018-9.

[50] Y. F. Zhang, J. Zheng, J. X. Yu, and H. T. He, "Impact of strain rate on the hardness and elastic modulus of human tooth enamel," *Journal of the Mechanical Behavior of Biomedical Materials*, vol. 78, pp. 491-495, 2018/02/01/ 2018, doi: https://doi.org/10.1016/j.jmbbm.2017.12.011.

[51] J. Hutchinson and A. Evans, "Simulation of the High Temperature Impression of Thermal Barrier Coatings with Columnar Microstructure," *Acta Materialia*, vol. 52, pp. 565-571, 02/09 2004, doi: https://doi.org/10.1016/j.actamat.2003.09.047.

[52] R. Wellman and J. Nicholls, "A review of the erosion of thermal barrier coatings," *Journal of Physics D: Applied Physics*, vol. 40, p. R293, 08/03 2007, doi: https://doi.org/10.1088/0022-3727/40/16/R01.

[53] A. C. Fischer-Cripps, *Nanoindentation*. Springer New York, 2013.

[54] MicroMaterials, "NanoTest® Vantage," ed. Willow House, Yale Business Village, Ellice Way, Wrexham, LL137YL, UK.

[55] I. Farooq and Z. Farooq, "Air Abrasion: Truly Minimally Invasive Technique," *International Journal of Prosthodontics and Restorative Dentistry*, pp. 105-107, 07/01 2011, doi: https://doi.org/10.5005/jp-journals-10019-1019.

[56] D. M. Ebenstein and L. A. Pruitt, "Nanoindentation of biological materials," *Nano Today*, vol. 1, no. 3, pp. 26-33, 2006/08/01/ 2006, doi: https://doi.org/10.1016/S1748-0132(06)70077-9.

[57] L. Qian and H. Zhao, "Nanoindentation of soft biological materials," *Micromachines*, vol. 9, no. 12, p. 654, 2018, doi: https://dx.doi.org/10.3390%2Fmi9120654.

[58] MicroMaterials, "Liquid Cell - MicroMaterials." [Online]. Available: https://www.micromaterials.co.uk/environment/liquid-cell/.

[59] Y.-T. Cheng and C.-M. Cheng, "Scaling, Dimensional Analysis, and Indentation Measurements," *Materials Science and Engineering: R: Reports*, vol. 44, pp. 91-149, 08/01 2004, doi: https://doi.org/10.1016/j.mser.2004.05.001.

[60] C. Chang, M. Garrido, J. Ruiz-Hervias, Z. Zhang, and L.-l. Zhang, "Representative stress-strain curve by spherical indentation on elastic-plastic materials," *Advances in Materials Science and Engineering*, vol. 2018, 2018, doi: https://doi.org/10.1155/2018/8316384.

[61] D. Tabor, *The Hardness of Metals*. OUP Oxford, 2000.

[62] J. Wheeler, "Nanoindentation Under Dynamic Conditions," 2009.

[63] D. Tabor, "A simple theory of static and dynamic hardness," *Proceedings of the Royal Society of London. Series A. Mathematical and Physical Sciences*, vol. 192, no. 1029, pp. 247-274, 1948, doi: https://doi.org/10.1098/rspa.1948.0008.

[64] J. M. Wheeler and A. G. Gunner, "Analysis of failure modes under nano-impact fatigue of coatings via high-speed sampling," *Surface and Coatings Technology*, vol. 232, pp. 264-268, 2013/10/15/ 2013, doi: https://doi.org/10.1016/j.surfcoat.2013.05.028.

[65] A. C. Barone *et al.*, "Calibration issues for nanoindentation experiments: Direct atomic force microscopy measurements and indirect methods," *Microscopy Research and Technique*, vol. 73, no. 10, pp. 996-1004, 2010/10/01 2010, doi: https://doi.org/10.1002/jemt.20850.

[66] C. Clapham, J. Nicholson, and J. R. Nicholson, *The Concise Oxford Dictionary of Mathematics*. OUP Oxford, 2014.

[67] G. Constantinides, C. Tweedie, N. Savva, J. Smith, and K. Van Vliet, "Quantitative Impact Testing of Energy Dissipation at Surfaces," *Experimental Mechanics*, vol. 49, pp. 511-522, 08/01 2008, doi: https://doi.org/10.1007/s11340-008-9198-1.

[68] B. D. Beake *et al.*, "Investigating the fracture resistance and adhesion of DLC films with micro-impact testing," *Diamond and Related Materials*, vol. 11, no. 8, pp. 1606-1609, 2002/08/01/ 2002, doi: https://doi.org/10.1016/S0925-9635(02)00107-3.

[69] J. Zhang, G. L. Niebur, and T. C. Ovaert, "Mechanical property determination of bone through nano- and micro-indentation testing and finite element simulation," *Journal of Biomechanics*, vol. 41, no. 2, pp. 267-275, 2008/01/01/ 2008, doi: https://doi.org/10.1016/j.jbiomech.2007.09.019.

[70] F. Linde, P. Nørgaard, I. Hvid, A. Odgaard, and K. Søballe, "Mechanical properties of trabecular bone. Dependency on strain rate," *Journal of Biomechanics*, vol. 24, no. 9, pp. 803-809, 1991/01/01/ 1991, doi: https://doi.org/10.1016/0021-9290(91)90305-7.

[71] Z. J. Cheng, X. M. Wang, F. Z. Cui, J. Ge, and J. X. Yan, "The enamel softening and loss during early erosion studied by AFM, SEM and nanoindentation," (in eng), *Biomed Mater*, vol. 4, no. 1, p. 015020, Feb 2009, doi: https://doi.org/10.1088/1748-6041/4/1/015020.

[72] M. Baig, R. Cook, J. Pratten, and R. Wood, "The effect of shape and size distribution of abrasive particles on the volume loss of enamel using micro-abrasion," *Wear*, vol. 448-449, p. 203212, 2020/05/15/ 2020, doi: https://doi.org/10.1016/j.wear.2020.203212.

[73] M. Granke, M. D. Does, and J. S. Nyman, "The Role of Water Compartments in the Material Properties of Cortical Bone," (in eng), *Calcif Tissue Int*, vol. 97, no. 3, pp. 292-307, 2015, doi: https://doi.org/10.1007/s00223-015-9977-5.

[74] J. S. Nyman, A. Roy, X. Shen, R. L. Acuna, J. H. Tyler, and X. Wang, "The influence of water removal on the strength and toughness of cortical bone," (in eng), *Journal of biomechanics*, vol. 39, no. 5, pp. 931-938, 2006, doi: https://doi.org/10.1016/j.jbiomech.2005.01.012.

[75] S. N. White, W. Luo, M. L. Paine, H. Fong, M. Sarikaya, and M. L. Snead, "Biological Organization of Hydroxyapatite Crystallites into a Fibrous Continuum Toughens and

Controls Anisotropy in Human Enamel," *Journal of Dental Research*, vol. 80, no. 1, pp. 321-326, 2001/01/01 2001, doi: https://doi.org/10.1177/00220345010800010501.

APPENDIX A MULTIPLE REGRESSION ANALYSIS USING STRAIN RATE AND D/D RATIO

Multiple regression analysis was carried out using *D/d* ratio values and strain rate values as predictors to estimate values of the dependent variables. The analysis was carried out in Microsoft Excel. An ANOVA test was also done, and differences with a p value of <0.05 deemed as statistically significant. All four analyses had a p value of <0.05. Correlation coefficients, R^2 values, linear regression coefficients and the final linear regression equations for each dependent variable are summarised in the tables below.

Table A.1: Multiple regression analysis to predict dynamic hardness (*DH*)

Correlation coefficient		*D/d* ratio	StrainRate	*DH*	
	D/d ratio	1			
	StrainRate	-0.79822	1		
	DH	-0.73439	0.957752	1	
Regression Statistics	R Square		0.919787		
	Adjusted R Square		0.919333		
Coefficients		Coefficients	Standard Error	t Stat	P-value
	Intercept	-11.5093	1.311818	-8.77352	7.51E-17
	D/d ratio	0.352263	0.106235	3.315894	0.001008
	StrainRate	1.841574	0.045006	40.91878	4.8E-136
Linear regression equation	**Predicted_*DH* = 1.8415749*(StrainRate) + 0.352263*(D/d ratio) - 11.5093**				

Table A.2: Multiple regression analysis to predict dynamic depth (h_{dyn})

Correlation coefficient		*D/d* ratio	StrainRate	h_{dyn}	
	D/d ratio	1			
	StrainRate	-0.80411	1		
	h_{dyn}	-0.5287	0.603979	1	
Regression Statistics	R Square		0.370031		
	Adjusted R Square		0.366389		
Coefficients		Coefficients	Standard Error	t Stat	P-value
	Intercept	232.8883	19.55323	11.91048	1.21E-27
	D/d ratio	-2.79828	1.649395	-1.69655	0.090681
	StrainRate	4.61427	0.654467	7.050422	9.74E-12
Linear regression equation	**Predicted_h_{dyn} = 4.61427*(StrainRate) - 2.79828*(D/d ratio) + 232.8883**				

Table A.3: Multiple regression analysis to predict Impact energy (E_{impact})

Correlation coefficient		*D/d* ratio	StrainRate	E_{impact}	
	D/d ratio	1			
	StrainRate	-0.79858	1		
	E_{impact}	-0.04724	0.422716	1	
Regression Statistics	R Square		0.411356		
	Adjusted R Square		0.408031		
Coefficients		Coefficients	Standard Error	t Stat	P-value
	Intercept	5.619539	1.072241	5.240931	2.75E-07
	D/d ratio	1.032503	0.087287	11.82888	1.97E-27
	StrainRate	0.571121	0.03641	15.68567	1.8E-42
Linear regression equation	**Predicted_E_{impact} = 0.571121*(StrainRate) + 1.032503*(D/d ratio) + 5.619539**				

Table A.4: Multiple regression analysis to predict coefficient of restitution (*CoR*)

Correlation coefficient		*D/d* ratio	StrainRate	*CoR*	
	D/d ratio	1			
	StrainRate	-0.799571216	1		
	CoR	0.833227794	-0.8530465	1	
Regression Statistics	R Square		0.791034996		
	Adjusted R Square		0.789827106		
Coefficients		Coefficients	Standard Error	t Stat	P-value
	Intercept	0.661227723	0.005704832	115.9066139	6.4E-279
	D/d ratio	0.004899682	0.000478415	10.24149011	1.12E-21
	StrainRate	-0.002426082	0.000191665	-12.65795801	1.94E-30
Linear regression equation	**Predicted_*CoR* = -0.002426082*(StrainRate) + 0.004899682*(D/d ratio) + 0.661227723**				

APPENDIX B TRIALS WITH LIQUID CELL APPARATUS

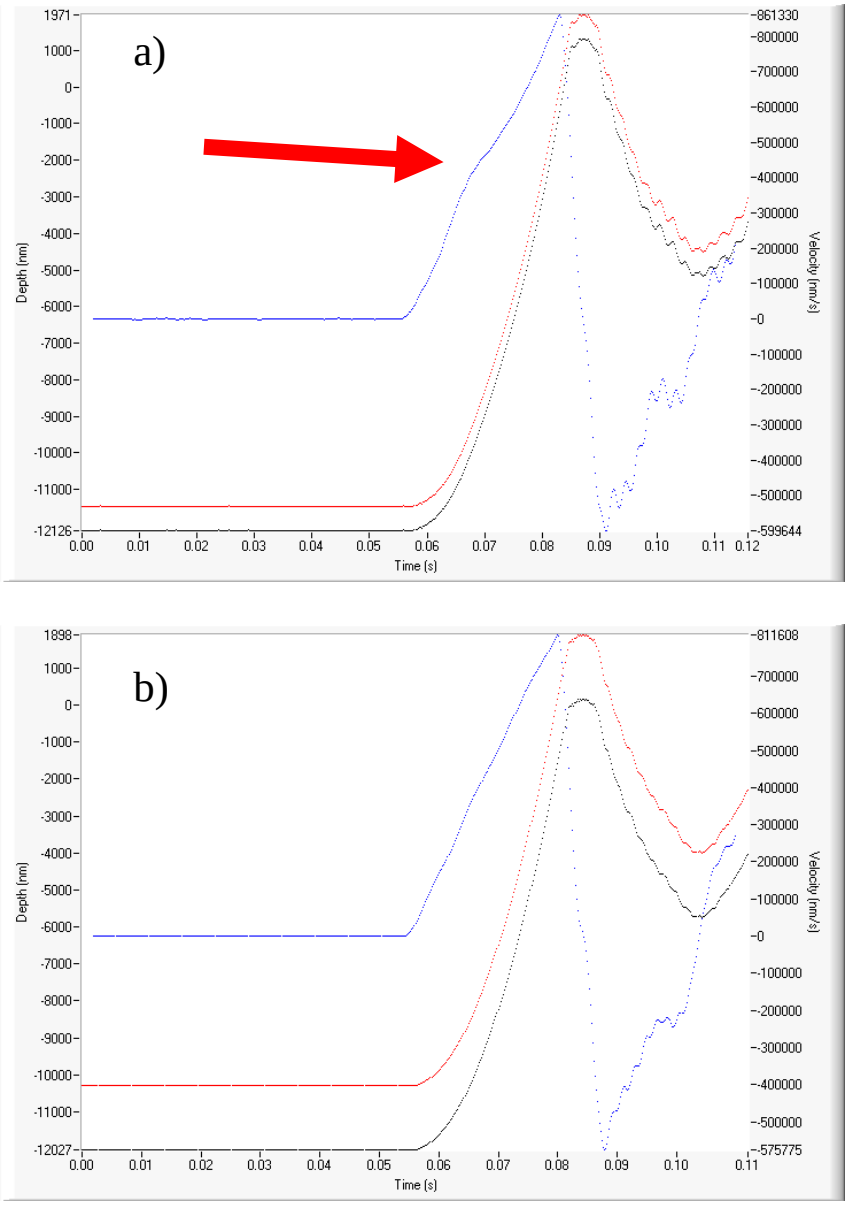

Figure B.1: Depth-Velocity-Time plots for nanoimpact tests using 100µm tip at 12µm flight distance with test carried out in a) liquid cell apparatus and b) air (dry conditions). Hump indicated by red arrow.

An example of the fluid interaction 'hump' is shown in Figure A.1(a). This hump was seen in nearly every nanoimpact carried out with the liquid cell apparatus.